



Influence of deep gaps on laminar–turbulent transition in two-dimensional boundary layers at subsonic Mach numbers

Steffen Risius^{1,2} · Marco Costantini¹ · Christian Klein¹

Received: 8 February 2023 / Revised: 7 August 2023 / Accepted: 12 September 2023 / Published online: 28 October 2023
© The Author(s) 2023

Abstract

Systematic experimental investigations on the influence of deep gaps on the location of laminar–turbulent transition are reported. The tests were conducted in the Cryogenic Ludwig–Tube Göttingen, a blow-down wind tunnel with good flow quality, at eight different unit Reynolds numbers ranging from $Re_1 = 17.5 \times 10^6 \text{ m}^{-1}$ to $80 \times 10^6 \text{ m}^{-1}$, three Mach numbers, $M = 0.35, 0.50$ and 0.65 , and various pressure gradients. A flat-plate configuration, the extended two-dimensional wind tunnel model *PaLASTra* was modified in order to allow the installation of gaps with nominal widths of $30 \mu\text{m}$, $100 \mu\text{m}$ and $200 \mu\text{m}$ and a depth of $d = 9 \text{ mm}$. A maximum Reynolds number based on the gap width $Re_w = Re_1 \cdot w \approx 16,000$ was reached. Transition Reynolds numbers ranging from $Re_{tr} \approx 1 \times 10^6$ to 11×10^6 were measured, as a function of gap width, pressure gradient and Mach and Reynolds number. This systematic investigation facilitates a linear approximation of Re_{tr} dependent on the boundary layer shape factor H_{12} for various flow conditions and gap widths. It was therefore possible to conduct an investigation of Re_{tr} depending on Re_1 and the relative change of the transition location depending on the gap width w . Incompressible linear stability analysis was used to calculate amplification rates of Tollmien–Schlichting waves and determine critical N -factors by correlation with measured transition locations. The change in the critical N -factor ΔN by installation of the gap is investigated as a function of w and Re_w . It was found that a gap width of $30 \mu\text{m}$ reduces the critical N -factors in the range of $\Delta N \approx 0.5 \pm 0.25$, while gap widths of $100 \mu\text{m}$ and $200 \mu\text{m}$ reduce the critical N -factor in the range of $\Delta N \approx 1.5 \pm 1$. Interestingly, an increase in gap width from 100 to $200 \mu\text{m}$ was not found to induce smaller transition Reynolds numbers or reduced N -factors, which might be due to resonance effects.

1 Introduction

Fuel consumption of commercial transport aircraft can be reduced significantly by natural laminar flow (NLF) technology (Schrauf 2005). Over the last years laminar flow investigations have also received increasing attention from wind turbine manufacturers (Traphan et al. 2015; Reichstein et al. 2019).

It is well known that small surface imperfections, such as steps and gaps, can reduce laminar flow lengths significantly, which makes it necessary to define manufacturing and operating tolerances for NLF airfoils (Holmes et al. 1986; Arnal 1992; Masad and Nayfeh 1992; Wang and

Gaster 2005; Forte et al. 2015; Zahn and Rist 2015; Costantini et al. 2015b, 2016). Steps have been examined in various publications (see e.g. Perraud and Séraudie (2000); Wang and Gaster (2005); Crouch et al. (2006); Crouch and Kosorygin (2020); Edelmann and Rist (2015); Costantini (2016); Costantini et al. (2015b, 2016); Rius-Vidales and Kotsonis (2021)). In contrast gaps have been the focus of fewer studies. With respect to steps, in which the step height is the main geometric parameter to be examined (Costantini et al. 2015b), two parameters have to be considered in the study of gap effects on boundary-layer transition: the gap width w and the gap depth d . Most work focused on isolated, sharp-edged gaps, placed perpendicularly to a two-dimensional freestream without suction through the gap. Gaps with rounded edges were examined e.g. in Franco et al. (2018), Tocci et al. (2021a) and Tocci et al. (2021b), whereas the application of suction through the gap for transition delay was considered even in the presence of steps in Zahn and Rist (2017) and Dimond et al. (2019, 2020, 2021). The influence of a suction region upstream of a gap was investigated

✉ Steffen Risius
steffen.risius@dlr.de

¹ German Aerospace Center (DLR), Bunsenstrasse 10,
37073 Göttingen, Germany

² Department of Mechanical Engineering, Kiel University
of Applied Sciences (FH Kiel), Grenzstraße 3, 24149 Kiel,
Germany

experimentally for example by Hensch et al. (2019) and Methel et al. (2022). Swept boundary layers studied in ONERA experiments were summarized in Beguet et al. (2017), whereas gaps in a three-dimensional configuration relevant for hybrid laminar flow control at flight conditions were examined by Franco et al. (2021).

The first experimental investigation on the influence of gaps on laminar–turbulent transition was conducted by Nenni and Gluyas (1966) who proposed a transition criterion based on the Reynolds number calculated with the gap width w . According to their findings transition occurs earlier at a ‘critical’ gap-width Reynolds number of $Re_w = U_\infty \cdot w/\nu = 15,000$. However, the term ‘critical’ is not well defined and very little detailed information about the experiments is known.

In the following subsections the results of earlier investigations with help of the ΔN method (Sect. 1.1) and Direct Numerical Simulations (DNS) are presented (Sect. 1.2), and also the motivation for the current study is described (Sect. 1.3).

1.1 The ΔN method

In two-dimensional laminar boundary layers developing on smooth surfaces in low-disturbance environment, Tollmien-Schlichting (T-S) waves are the dominant instability mechanism leading to transition. According to linear stability theory, the T-S waves grow exponentially in the linear amplification regime (Schlichting et al. 2006). The ratio between the T-S wave amplitude A at a streamwise position x and the initial amplitude A_0 at the initial position x_0 is given by $A/A_0 = e^N$, where N is the so-called amplification factor. Based on linear stability theory, the e^N method assumes that transition occurs when a critical N -factor N_{tr} is reached (van Ingen 1956; Smith and Gamberoni 1956). The critical N -factor N_{tr} is typically determined via correlation of the results of linear stability computations with experimental transition data. In a manner similar to that proposed for steps (Wang and Gaster 2005; Crouch et al. 2006; Edelmann and Rist 2015) a ΔN method was also considered to model the effect of gaps on boundary-layer stability (Beguet et al. 2017; Crouch 2022; Crouch et al. 2022). In the presence of steps or gaps, the ΔN method models the additional amplification of the T-S waves caused by the imperfection as an increase of the N -factor (ΔN) as compared to the N -factor of the smooth surface.

Experimental and numerical studies conducted at ONERA in subsonic flows on a flat plate and on airfoils are summarized in Beguet et al. (2017). They give a detailed description of the ΔN method and differentiate between ΔN_{peak} and ΔN_{far} . Hereby, ΔN_{peak} represents a drastic amplification shortly downstream of the roughness, which leads to an increase of T-S waves with high frequencies. ΔN_{far}

represents a shift from the reference N -factor curve by amplifying low-frequency T-S waves over a wide chordwise extent, which induces a progressive upstream movement of the transition position. Beguet et al. (2017) show promising results of the ΔN method to predict the influence of gaps. However, they state that they found it difficult to treat deep gaps due to convergence issues of the laminar Navier–Stokes solver; they also stress the missing experimental verification of the ΔN method at flow velocities larger than $M = 0.3$ as well as the necessity to investigate pressure gradient effects.

Crouch et al. (2022) and Crouch (2022) recently investigated gaps with different depth to width ratios d/w mounted on a flat plate in a low-speed flow with an imposed pressure distribution. Two different pressure gradients (favourable and adverse) were examined by varying the gap position while keeping the pressure distribution unchanged. Based on their results they develop a model which describes the change of the limiting N -factor as a function of depth and width of the gap. In line with earlier work on steps (Wang and Gaster 2005; Crouch et al. 2006; Crouch and Kosorygin 2020) the gap-induced increment ΔN was modelled as a uniform offset, which was determined by correlating the N -factor distributions for the reference (i.e. smooth) surface with the transition locations measured with gaps. They found a dependency of ΔN on the gap width (w/δ_1) and depth (d/δ_1) normalized by the boundary-layer displacement thickness at the gap location δ_1 computed in the absence of the gaps. While for shallow gaps with $d/w < 0.028$ the variation of the N -factor was observed to depend only on the gap depth, ΔN depends exclusively on gap width for deep gaps. The results obtained in the two different pressure gradients were shown to be in reasonable agreement, with a bias towards smaller ΔN values in the case of the favourable pressure gradient.

1.2 Direct numerical simulations at a single Mach number

Zahn and Rist (2015) carried out Direct Numerical Simulations of a laminar flow over a gap at a Mach number of $M = 0.6$ at zero pressure gradient. Excitation of acoustic waves was observed inside the gap, in a manner similar to that of acoustic waves occurring in organ pipes. They found that in deep gaps with $w/d \ll 1$ and a width much smaller than the wave length of the incoming (original) T-S waves, the standing wave inside the gap leads to the generation of new T-S waves downstream of the gap, which may interact with the original T-S waves and cause a change of the transition location. Depending on the gap depth, the impact of the gaps on boundary-layer transition was predicted to be either significant or negligible. The change of the T-S amplification for different gap depths was explained with both the resonance effect inside the gap and the superposition of the

Table 1 Characteristic parameters of the investigated gaps in this study

| Nominal gap width | 30 μm | 100 μm | 200 μm |
|---------------------------------------|------------------|-------------------|-------------------|
| Real gap width: w [μm] | 34.9 | 105.1 | 200.5 |
| w/d | 0.0039 | 0.0117 | 0.0223 |
| d/w | 257.9 | 85.6 | 44.9 |
| $w/\delta_1 \approx$ | 0.34–0.78 | 0.91–2.03 | 1.75–4.02 |
| $d/\delta_1 \approx$ | 86–200 | 78–174 | 78–180 |
| $Re_w/10^3 \approx$ | 0.67–3.07 | 1.93–8.10 | 3.52–16.12 |
| $Re_d/10^3 \approx$ | 172–793 | 165–694 | 158–724 |

original T-S waves with the gap-generated, new T-S wave. Zahn and Rist (2015) considered only one gap width and conclude that other gap widths should be investigated, which might lead to different values of ΔN .

1.3 Motivation and features of the current study

Except for the last cited publications, most earlier experimental studies considered low-speed boundary layers ($M < 0.3$) at relatively small unit Reynolds numbers ($Re_1 < 5 \times 10^6 \text{ m}^{-1}$) and relatively shallow gaps ($d/w < 1$). Moreover, most earlier work examined flat-plate configurations at zero pressure gradient. Beguet et al. (2017) explicitly state that the pressure gradient effect should be further investigated as well as the effects of compressibility and of larger gap depths ($d/w > 1$).

This study investigates the influence of sharp edged gaps with a depth of 9 mm which are more than 45 times deeper than their width. The w/d -ratio is therefore much smaller than unity. As compared to previous work, the present gaps may be considered as ‘very deep.’ Nevertheless, they are relevant for aircraft configurations as an imperfect joint of wing parts (e.g. by integration of high-lift devices) may be similar to the gaps considered here. The influence of gap width on the transition location is systematically investigated for three different gap widths, three different subsonic Mach numbers ($M = 0.35, 0.50$ and 0.65), eight unit Reynolds numbers in the range of $Re_1 = 17.5 \times 10^6 \text{ m}^{-1}$ to $80 \times 10^6 \text{ m}^{-1}$ and different streamwise pressure gradients. This study focuses on favourable pressure gradients, which are the most relevant for NLF surfaces. Nevertheless, also zero and adverse pressure gradients are examined. The nominal widths of the gaps are $w = 30 \mu\text{m}$, $100 \mu\text{m}$ and $200 \mu\text{m}$. The boundary layer thickness at the gap location in the absence of the gap varies between $\delta_1 \approx 45 \mu\text{m}$ and $116 \mu\text{m}$. That results in normalized gap widths that vary between $w/\delta_1 \approx 0.34$ to 4.02 , which correspond to a gap-width Reynolds number in the range of $Re_w = (U_\infty w/\nu) \approx 670$ to 16120 . The gap depth of all cases is $d = 9 \text{ mm}$, resulting in a width-to-depth ratio

of $w/d \approx 3.9 \times 10^{-3}$ to 22×10^{-3} (depth-to-width ratio of $d/w \approx 44.9$ to 257.9), as shown in detail in Table 1.

The systematic variation of flow parameters is based on the study of unit Reynolds numbers, Mach numbers and pressure gradients for the reference (smooth, i.e. gap-free) surface reported by Risius et al. (2018b). Compared to earlier investigations of the influence of gaps on the transition location, this systematic approach allows a quantification of the effect of the gap in terms of the transition Reynolds number as a function of non-dimensional gap parameters, pressure gradient parameters (characterized here by the incompressible shape factor) and the unit Reynolds number for different Mach numbers.

In parallel to Risius et al. (2018b), also boundary layer calculations and a linear stability analysis were performed on the basis of the pressure and temperature distributions measured on the investigated surface. This approach allowed to obtain the distributions of the amplification factors of T-S waves and thus the determination of the gap-induced ΔN , following the procedure proposed by Crouch (2022); Crouch et al. (2022), i.e. via correlation of the computed N -factor distributions with the transition locations measured in the experiments with and without gaps.

The investigated gap dimensions were chosen for two reasons. On the one hand, the three examined gap widths allowed the achievement of an overlap in the non-dimensional gap parameters ($w/\delta_1, Re_w$) for different dimensional gap widths w by varying the unit Reynolds number (see Sect. 4). On the other hand, the investigated gap dimensions (in non-dimensional terms) are representative for the size of the gaps that may occur on commercial transport aircraft wings, and thus enable the transfer of the knowledge gained in fundamental research to applied aerodynamics. In the case of a single-aisle, mid-range subsonic transport aircraft, the mean aerodynamic chord length is about 4–4.2 m (EASA 2017, 2023), which is about 20 times the chord length of the investigated wind tunnel model. Multiplication of the nominal gap dimensions with a factor of 20 leads to a gap depth in the range of about 18 mm, while the corresponding gap widths would be about 0.6 mm, 2 mm and 4 mm at the wing of the aforementioned transport aircraft.

2 Materials and methods

The experimental setup, the boundary-layer flow and the numerical analysis will be described in this section. It is kept as short as possible, while further information can be found in the cited literature below.

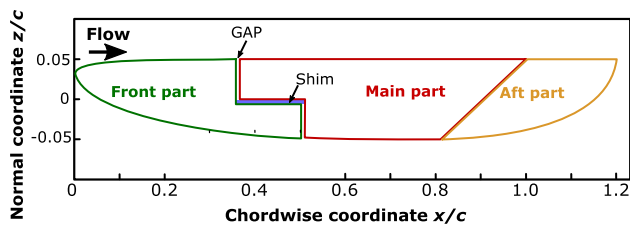


Fig. 1 Side view of the *PaLASTra* model with three parts. The gap is located between the front and the main part at $x_G/c = 0.35$. The original chord length of $c = 0.2$ m is used for normalization of the chordwise coordinate, in line with previous work (Costantini et al. 2015b; Costantini 2016; Costantini et al. 2016, 2018; Risius et al. 2018b; Dimond et al. 2019, 2020, 2021)

2.1 The Cryogenic Ludwig–Tube Göttingen

The experiments were performed in the transonic Cryogenic Ludwig–Tube Göttingen (KRG) (Rosemann 1997; Koch 2004). The blow-down wind tunnel is operated intermittently with gaseous nitrogen as driving gas and has good flow quality. The total temperature turbulence level¹, Tu_{T_0} , in the centre of the test section, is lower than 0.04 % at Mach number $M = 0.8$, unit Reynolds number $Re_1 = 30 \times 10^6 \text{ m}^{-1}$ and charge temperature $T_c \approx 282 \text{ K}$, and it decreases with lower Mach numbers. The mass flux turbulence level¹, $Tu_{\rho u}$, in the centre of the test section is approximately 0.06 % at $M = 0.8$, $T_c \approx 283 \text{ K}$ and $30 \times 10^6 < Re_1 < 77 \times 10^6 \text{ m}^{-1}$; it increases slightly at lower Mach numbers, but remains smaller than 0.08 % (Koch 2004). In order to guarantee an interference-free flow around the wind tunnel model, the upper and lower test section walls were adapted (Rosemann 1997). The uncertainties in the inflow Mach and Reynolds numbers in the present work were within $M = \pm 0.002$ and $Re_1 = \pm 0.25 \times 10^6 \text{ m}^{-1}$. In blow-down cryogenic facilities, like KRG, a negative temperature step occurs due to expansion of the gaseous nitrogen after opening the fast-acting valve. The resulting impact of the non-adiabatic thermal boundary condition at the model surface was investigated in detail by Costantini et al. (2015a, 2018) and integrated into the boundary layer calculations (Risius et al. 2018b).

2.2 The *PaLASTra* wind tunnel model

The wind tunnel model used for the present study was the two-dimensional *PaLASTra* model. The model is composed of three parts which are connected with the help of shims and bolts integrated into the model (see Fig. 1). This specific manufacturing of the model allows the installation of

gaps with high accuracy into the model between the front and the main part at $x_G/c = 0.35$ of the upper surface. During the first measurement campaigns only the front and the main part of the model were used, causing a large separation region behind the model, which results in strong pressure fluctuations that influence the measured transition locations (Costantini et al. 2015a; Costantini 2016; Costantini et al. 2016, 2018). In later measurement campaigns the complete model including the aft-part was used, effectively reducing separation-induced pressure fluctuations (Risius et al. 2018a, b; Dimond et al. 2019, 2020, 2021).

The model cross section was designed to achieve a nearly uniform streamwise pressure gradient on the model upper surface, which is the one of main interests in this work. In Risius et al. (2018b), the computed profile of the normalized streamwise velocity component was compared at different flow conditions, and an almost self-similar boundary-layer profile was found downstream of $x/c = 5\%$, under the assumption of complete laminarity.

In order to assure the correct installation of the gap with minimal variation, the gap width was measured systematically along the span with a profilometer. The standard deviation of the measured gap widths is in the range of $5 \mu\text{m}$. As reported in Table 1, the nominal gap widths of $30 \mu\text{m}$, $100 \mu\text{m}$ and $200 \mu\text{m}$ deviate slightly from the actual gap widths of $34.9 \mu\text{m}$, $105.1 \mu\text{m}$ and $200.5 \mu\text{m}$. The actual gap widths are considered for the evaluation of the gap-width parameters (w/d , Re_w , etc.), while the nominal gap widths are used throughout the article to refer to the different model configurations.

In earlier studies a flow through the model has been used to investigate the influence on laminar turbulent transition of boundary-layer suction through the gap (Dimond et al. 2019, 2020, 2021). However, in the setup used in this study an inner flow was prevented by a tight installation of the complete shim and additional sealing at the bottom of the model.

2.3 Measurement of the pressure distribution

The model was equipped with a row of pressure taps to measure the surface pressure distribution (Costantini et al. 2015b; Costantini 2016; Costantini et al. 2016, 2018; Dimond et al. 2019; Risius et al. 2018a). Typical pressure distributions of the upper side of the modified *PaLASTra* model are shown in Figs. 2 and 3 for different model configurations. As introduced above, the pressure gradient is essentially uniform over a large portion of the upper surface. Only around $x/c = 0.35$ the pressure coefficients show some slight variations from an ideally smooth distribution, which are due to the connection between the model parts (Costantini et al. 2015b; Costantini 2016; Costantini et al. 2018). However, it can be observed in Figs. 2 and 3 that the pressure distributions of all gap widths are

¹ The turbulence level of a quantity x is defined as $Tu_x = \sqrt{(x - \bar{x})^2 / \bar{x}} = x_{RMS} / \bar{x}$, where \bar{x} is the temporal average of x and x_{RMS} is the RMS of the fluctuations.

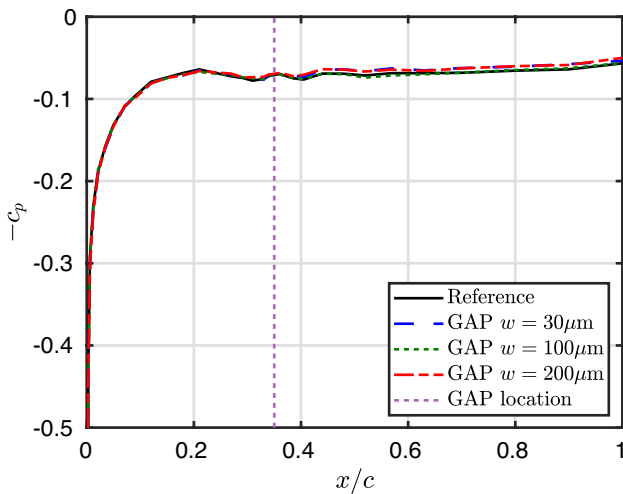


Fig. 2 Exemplary distribution of pressure coefficient, c_p , on model upper side at $Re_1 = 17.5 \times 10^6 \text{ m}^{-1}$, $M = 0.35$, $H_{12} \approx 2.6$ with an angle-of-attack of -1.0°

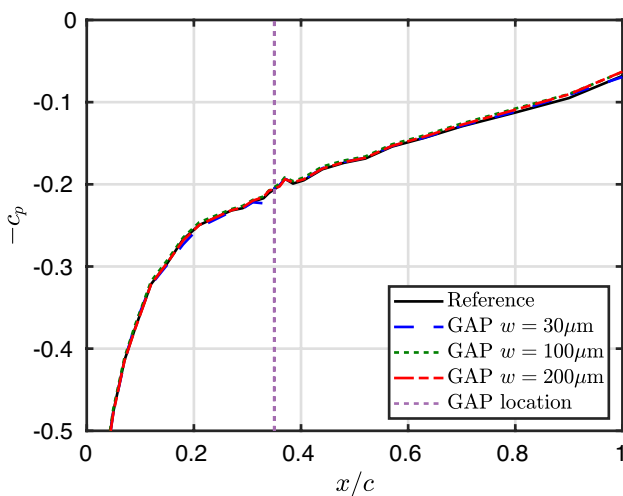


Fig. 3 Exemplary distribution of pressure coefficient, c_p , on model upper side at $Re_1 = 50 \times 10^6 \text{ m}^{-1}$, $M = 0.65$, $H_{12} \approx 2.5$ with an angle-of-attack of -3.5°

almost identical to the pressure distributions of the reference configuration, provided that the flow conditions are reproduced. It should be emphasized here that the spatial resolution of the surface pressure measurements was not sufficient to measure the very strong pressure gradients occurring in close proximity of the gaps (Zahn and Rist 2015; Beguet et al. 2017). In fact, the slight variation of the pressure distribution in Fig. 2 is not due to the installation of the gaps, but mainly caused by the slight variation in the test conditions between the different runs. However, due to the systematic variation of the angle-of-attack at

each flow condition, a linear approximation was able to compensate for these small deviations as described in Sect. 3.1.

2.4 Temperature-sensitive paint measurement

Non-intrusive global measurement of the surface temperature distribution was carried out using a Temperature-Sensitive Paint (TSP) to optically measure the surface temperature distribution—and thus boundary-layer transition—on the model upper surface (Liu et al. 2021). TSP formulation, surface quality, acquisition and evaluation of the TSP images were already described (Ondrus et al. 2015; Costantini et al. 2018; Risius 2018). After the first measurement campaign the optical setup was improved: in particular, enhancements were made in the data acquisition by installation of new LEDs to illuminate the TSP, leading to an increased temporal resolution and signal-to-noise ratio (SNR) of TSP result images (Risius et al. 2015). Furthermore, a new camera setup was developed; it was used during the later entries of the *PaLASTra* model and enabled increased spatial resolution, temporal resolution and SNR in the result images (Risius 2014, 2018). The effect of the improved optical setup can be seen by comparing the first transition result on the very left of Fig. 4, which was taken with the old optical setup, and the three results on the right of Fig. 4, which were acquired with the improved optical setup and show a better signal-to-noise ratio.

Each TSP image in Fig. 4 shows a laminar region on the left (light grey) and a turbulent region on the right (dark). A turbulent wedge in the mid-span domain is caused by pressure taps in the span-wise centre of the model, which was excluded from transition detection. The measured transition locations are $x_T/c = 92.0\%$, 86.5% , 77.2% and 76.5% (from left to right).

The transition detection was carried out over almost the complete span at up to 300 separate spanwise sections by the maximal gradient technique (Costantini et al. 2021). For each section the maximum intensity gradient in flow direction was determined and marked by a red dot which highlights the determined transition location. Side wall effects (visible at top and bottom of Fig. 4) and turbulent wedges (in the middle of Fig. 4) caused by surface contamination or pressure taps were excluded from the transition detection (Risius et al. 2018b; Costantini et al. 2021). The RMS of the variation in transition location along the span was determined for each data point and used to quantify the measurement uncertainty of the transition location, which was typically within $\Delta x/c = 1\%$.

The series of TSP results shown in Fig. 4 were obtained for different gap widths. The result image of the reference configuration can be seen on the very left of the series in Fig. 4. In this case the transition location is close to the end of the model (with $x_T/c = 92.0\%$) and it moves upstream

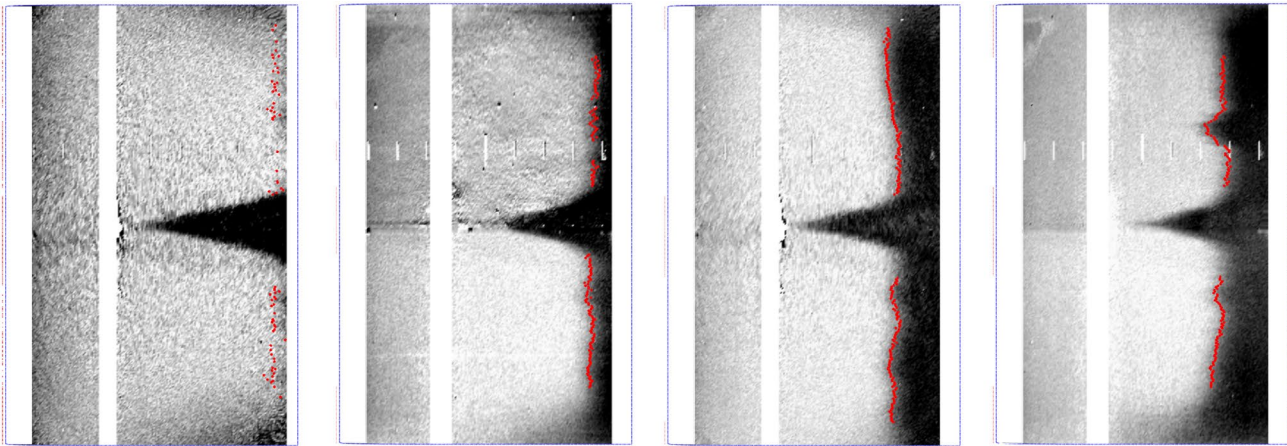


Fig. 4 TSP results on model upper side for four configurations with $w = 0 \mu\text{m}$, $30 \mu\text{m}$, $100 \mu\text{m}$ and $200 \mu\text{m}$ (from left to right). The flow direction is from left to right, and the flow conditions are the same as in Figs. 2 and 5. The red dots indicate the detected transition locations by the maximal gradient technique at the undisturbed flow locations for each span-wise location (Costantini et al. 2021). The whit-

ened strips indicate metallic surfaces of the model where no TSP had been applied or locations where optical artefacts prohibit the detection of the transition location. Markers indicating every 10% chord are visualized by thin white lines on the starboard side. The resolution of the images is due to different optical setups as described in the text below

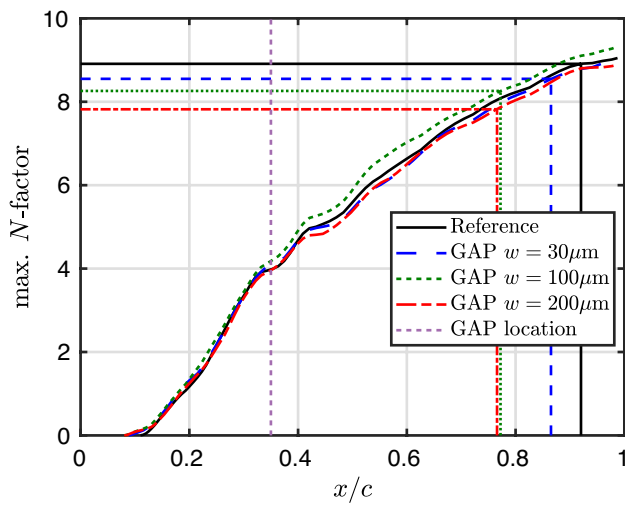


Fig. 5 Comparison of maximum N -factor distributions as a function of x/c for different gap sizes. Critical N -factors are determined at the measured transition location for each configuration. The flow conditions are $Re_1 = 17.5 \times 10^6 \text{ m}^{-1}$, $M = 0.35$ and $H_{12} \approx 2.6$, which are the same as in Figs. 2 and 4. The purple dotted line marks the location of the gap at $x_G/c = 0.35$

in three TSP images on the right with increasing gap sizes. However, the transition locations for $w = 100 \mu\text{m}$ (with $x_T/c = 77.2\%$) and $w = 200 \mu\text{m}$ (with $x_T/c = 76.5\%$) are very similar and are overlapping when the measurement uncertainties are considered. This observation for these two gap widths is common to all examined flow conditions and will be discussed later in this work.

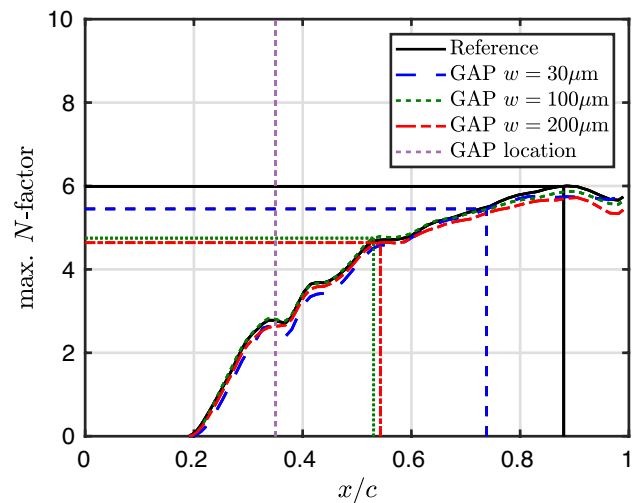


Fig. 6 Comparison of maximum N -factor distributions as a function of x/c for different gap sizes. The flow conditions are $Re_1 = 50 \times 10^6 \text{ m}^{-1}$, $M = 0.65$ and $H_{12} \approx 2.5$, which are the same as in Fig. 3. The purple dotted line marks the location of the gap at $x_G/c = 0.35$

In order to determine the surface temperature distribution on the upper side of the model, the TSP was calibrated in an external calibration chamber (Egami et al. 2012) and thermocouples integrated into the TSP layer were used to measure reference temperatures (Risius et al. 2018b). Surface temperature distributions in the streamwise direction, which were extracted from the TSP data at five spanwise sections, were averaged to obtain the streamwise surface temperature profile. The measured surface temperature and pressure distributions

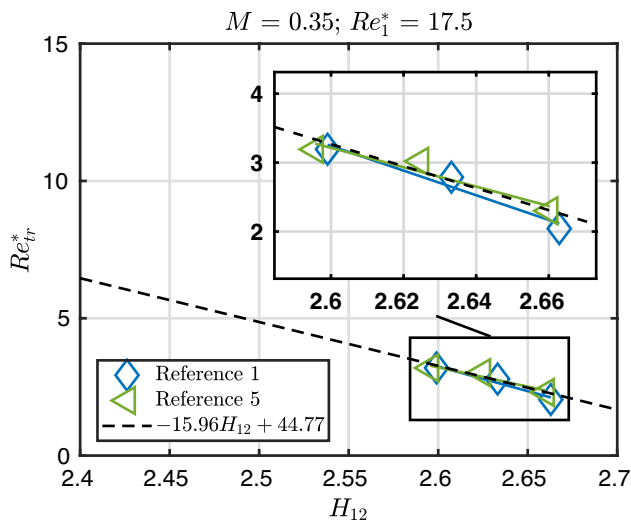


Fig. 7 Approximation of the influence of H_{12} on the transition Reynolds number for the reference configuration, which was measured in two different wind tunnel entries (labelled as ‘Reference 1’ and ‘Reference 5,’ where the number specifies the number of the wind tunnel entry). The fitted averaged function is shown as dashed black line. For better comparability the scale of H_{12} and Re_{tr}^* in the main figure was chosen to be identical with the scale in the figures in Appendix (Figs. 21, 24, 27, 30, 33, 36, 39, 42, 45, 48, 51, 54, 57). For better comparability a zoomed area is shown in this figure as an inset

were then used as inputs for boundary layer calculations, as described in Risius et al. (2018b) and summarized in the next section.

2.5 Boundary layer computations and stability analysis

Laminar boundary layer computations were performed using the compressible boundary layer solver *COCO* (Schrauf 1998), with a modification to incorporate the measured surface pressure and surface temperature distributions. *COCO* calculates a fully laminar boundary layer, which was used to determine incompressible displacement (δ_1) and momentum thickness (δ_2) of the laminar boundary layer. The average incompressible shape factor, $H_{12} = \delta_1/\delta_2$, was determined by averaging the incompressible shape factor curve between $24\% < x/c < 90\%$, in order to characterize the boundary layer velocity profile for varying streamwise pressure gradient. The selection of the incompressible shape factor as pressure gradient parameter is motivated in Risius et al. (2018b). H_{12} can be also used to calculate other pressure gradient parameters, such as the Hartree parameter (in the present case: $\beta_H = -0.687 \cdot H_{12} + 1.810$). A smaller value of H_{12} corresponds to a stronger favourable pressure gradient and a larger β_H , leading to an accelerated boundary layer.

Table 2 Intercepts, $h_{II,0}$, of reference configuration as a function of unit Reynolds number and Mach number (see Eq. II)

| Re_1^* | $M = 0.35$ | $M = 0.50$ | $M = 0.65$ |
|----------|------------|------------|------------|
| 17.5 | 44.77 | | |
| 22.5 | | 65.69 | |
| 30.0 | 83.28 | 72.70 | 76.08 |
| 40.0 | 94.88 | 107.36 | 110.23 |
| 50.0 | 118.81 | 123.36 | 130.14 |

Table 3 Slopes, $h_{II,1}$, of reference configuration as a function of unit Reynolds number and Mach number (see Eq. II). For each slope the number of evaluated data points is given in brackets

| Re_1^* | $M = 0.35$ | $M = 0.50$ | $M = 0.65$ |
|----------|-------------|-------------|-------------|
| 17.5 | -15.96 (6) | | |
| 22.5 | | -23.89 (12) | |
| 30.0 | -30.48 (18) | -26.44 (10) | -27.79 (11) |
| 40.0 | -34.78 (9) | -39.72 (6) | -41.02 (5) |
| 50.0 | -44.04 (11) | -45.91 (9) | -48.68 (7) |

Amplification factors of T-S waves for the computed boundary layer were determined by means of *LILLO* (Schrauf 2006). Based on the findings of Risius et al. (2018b), the incompressible N -factors are considered in the present analysis. This choice is also discussed in Sect. 5. The amplification factor N is determined by the envelope strategy, which uses the most amplified T-S wave at each transition location. According to

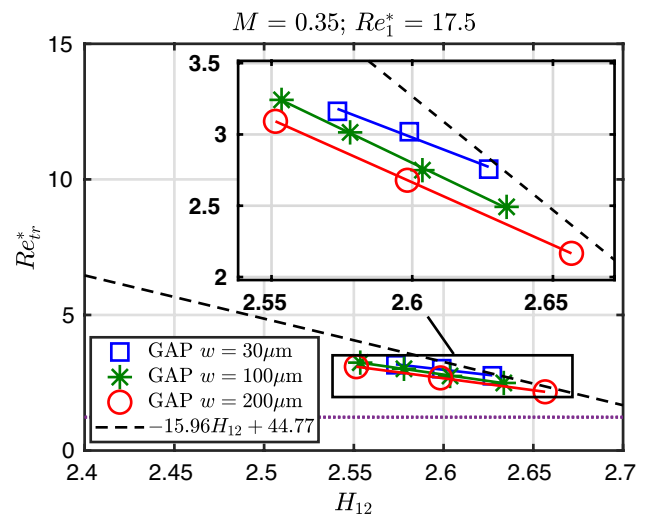


Fig. 8 Approximation of the influence of H_{12} on the transition Reynolds number for the configurations with gap. The fitted averaged function of the reference configuration is shown as dashed black line. The purple dotted line corresponds to the Reynolds number at the location of the gap at $x_G/c = 0.35$. For better comparability a zoomed area is shown in this figure as an inset

linear, local stability theory and the quasi-parallel flow assumption, incompressible stability computations were carried out, and their results were correlated with the measured transition location to assess critical N -factors, following the procedure by Crouch (2022); Crouch et al. (2022). A conceptual difference with the procedure of Crouch (2022); Crouch et al. (2022) is that the N -factor distributions were also computed in the presence of the gaps, as shown in Figs. 5 and 6. However, the N -factor distributions calculated for the different model configurations (with and without gaps) are very similar if the flow conditions are reproduced, since the computations of the N -factors are based on the measured pressure and temperature distributions only. As shown in Figs. 2 and 3, the pressure distributions measured for the different model configurations are essentially the same. Therefore, the present numerical simulations, based on the measured pressure distributions, miss the strong, localized disturbances induced by the gap. In practice, the procedure to calculate ΔN becomes analogous to that presented in Crouch (2022) and Crouch et al. (2022). For each configuration the transition location is determined with help of the TSP result and indicated by a vertical line in Fig. 5. The intercept of the transition location with the maximal N -factor curve is used to determine the critical N -factor (the horizontal lines in Fig. 5). This procedure is carried out for each measurement point of each configuration and used for the analysis as described in Sect. 5.

3 Analysis of the transition Reynolds number

The *PaLASTra* model was repeatedly tested in KRG with three different gap sizes in six separate measurement campaigns over a time span of two years. The reference configuration (without an installed gap) was re-tested in each measurement campaign. A good repeatability of the measured transition locations was observed, as shown exemplarily in Fig. 7 (for the first and fifth measurement campaign) and systematically in Appendix (Figs. 21, 24, 27, 30, 33, 36, 39, 42, 45, 48).

The influences of pressure gradient and unit Reynolds number on transition Reynolds number $Re_{tr} = x_T \cdot Re_1$ are analysed separately for each investigated Mach number: $M = 0.35, 0.50$ and 0.65 . Detailed results will be presented here for $M = 0.35$ and $Re_1 = 17.5 \times 10^6 \text{ m}$, while data from the other flow conditions are summarized in Tables 2 and 3 and presented in Figs. 21, 22, 23, 24, 25, 26, 27, 28, 29, 30, 31, 32, 33, 34, 35, 36, 37, 38, 39, 40, 41, 42, 43, 44, 45, 46, 47, 48, 49, 50, 51, 52, 53, 54, 55, 56, 57 in Appendix. For better readability, unit Reynolds numbers and transition Reynolds numbers

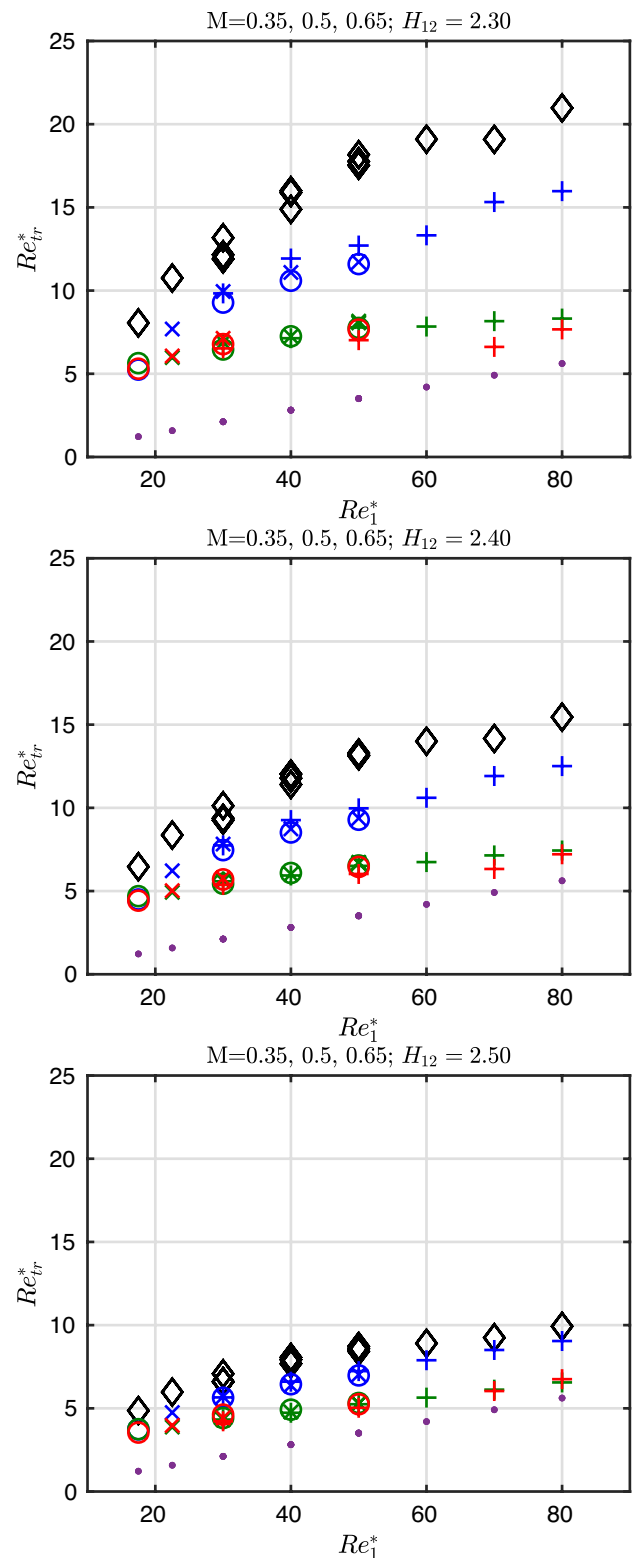


Fig. 9 Calculated transition Reynolds number Re_{tr} as a function of unit Reynolds number Re_1^* for all Mach numbers and different $H_{12} = 2.30$, $H_{12} = 2.40$ and $H_{12} = 2.50$ (from top to bottom). The purple dots mark the Reynolds number corresponding to the location of the gap. The legend is shown separately in Fig. 10

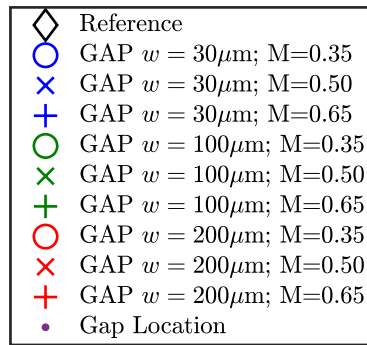


Fig. 10 Legend for Figs. 9, 12, 13, 17, 18, 19 and 20

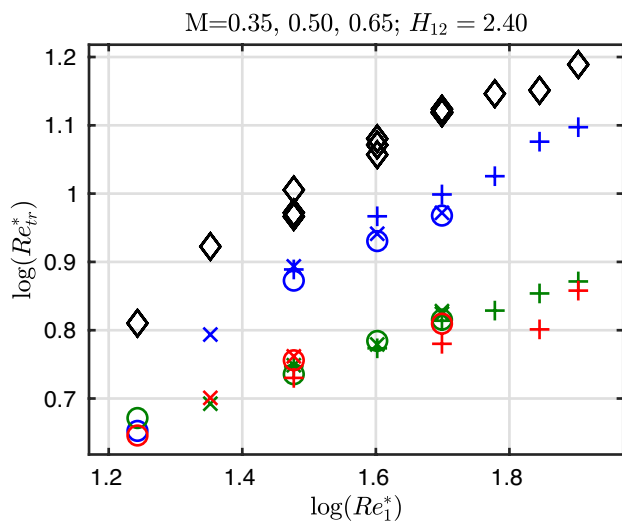


Fig. 11 Double-logarithmic plot of Reynolds number Re_{tr} as a function of unit Reynolds number Re_1^* for all Mach numbers and model configurations at $H_{12} = 2.40$. The legend is shown in Fig. 10

are normalized via $Re_1^* = Re_1 / (10^6 \text{ m})$ and $Re_{tr}^* = Re_{tr} / 10^6$, respectively.

3.1 Analysis of the pressure gradient and unit Reynolds number influence on the transition Reynolds number for the reference configuration

Following the analysis of Risius et al. (2018b) it was found that the transition Reynolds number increases almost linearly with a more pronounced favourable pressure gradient, corresponding to a shape factor decrease, as shown in

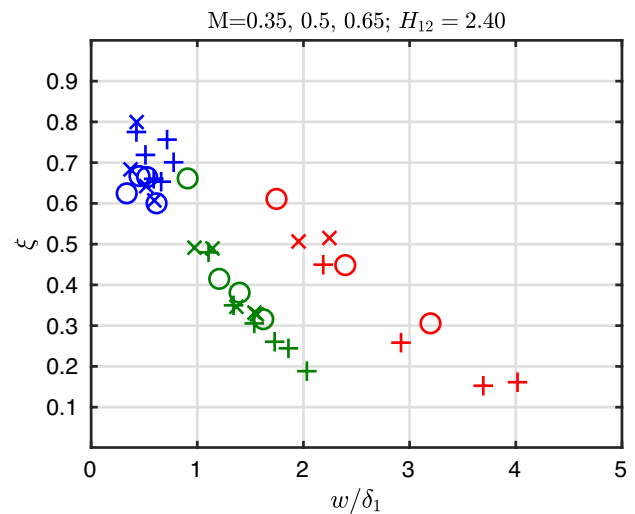


Fig. 12 The parameter ξ as a function of normalized gap width w/δ_1 for all Mach numbers and configurations with $H_{12} = 2.40$. The legend is shown separately in Fig. 10

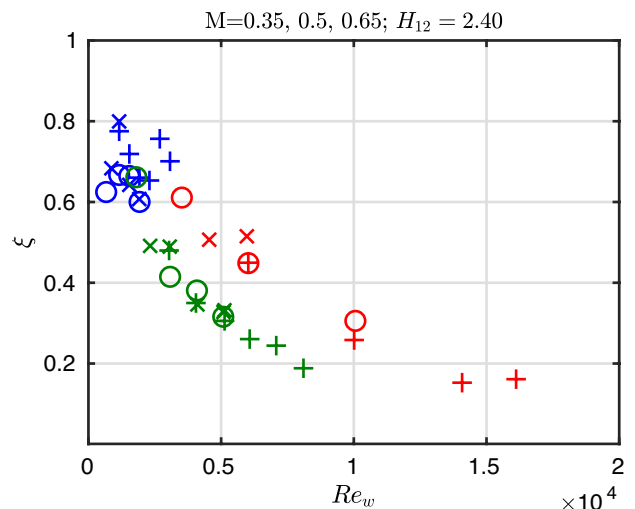


Fig. 13 The parameter ξ as a function of gap-width Reynolds number Re_w for all Mach numbers and configurations with $H_{12} = 2.40$. The legend is shown separately in Fig. 10

Fig. 7 for $M = 0.35$ and $Re_1^* = 17.5$ (chord Reynolds number $Re_c = 3.5 \times 10^6$). Consequently a linear function

$$Re_{tr}^* = h_{II,1} \cdot H_{12} + h_{II,0} \tag{II}$$

with an intercept, $h_{II,0}$, and a slope, $h_{II,1}$, was fitted through the data for each combination of Mach and Reynolds number (shown by solid lines of the corresponding colours in

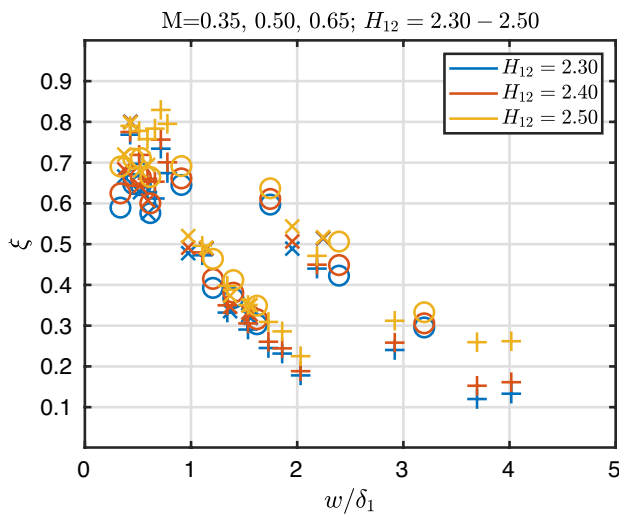


Fig. 14 The parameter ξ as a function of normalized gap width w/δ_1 for all Mach numbers with $H_{12} = 2.30$, $H_{12} = 2.40$ and $H_{12} = 2.50$. The legend of the Mach number is shown separately in Fig. 10, while the colour coding is shown in this figure

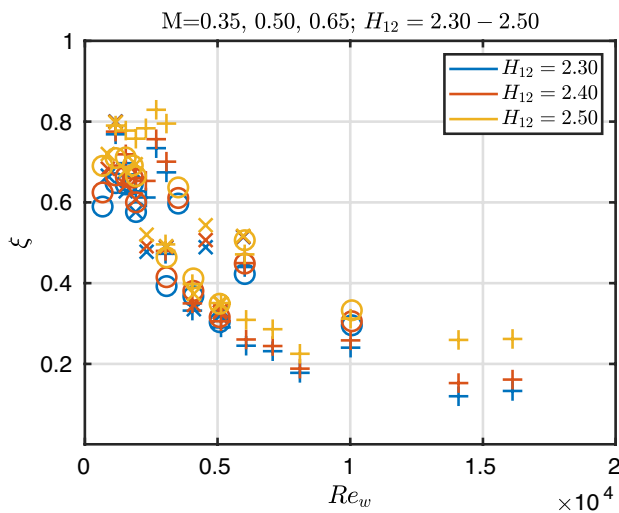


Fig. 15 The parameter ξ as a function of gap-width Reynolds number Re_w for all Mach numbers with $H_{12} = 2.30$, $H_{12} = 2.40$ and $H_{12} = 2.50$. The legend of the Mach number is shown separately in Fig. 10, while the colour coding is shown in this figure

Fig. 7).² Average slopes and intercepts were then calculated, and the fitted functions are shown as dashed lines in the corresponding figures. The measurement uncertainty of Re_{tr}^* is in the range of the symbol size or below, as discussed in Sect. 6.

² The labelling of the function and parameters corresponds to nomenclature of Risius et al. (2018b) on which the following analysis is based. It is kept identical for consistency and transparency.

The average coefficients $h_{II,0}$ and $h_{II,1}$ are summarized in Tables 2 and 3, respectively. In agreement with Risius et al. (2018b) it can be seen that for a fixed value of H_{12} an increasing unit Reynolds number leads to an increasing transition Reynolds number (Table 2). Furthermore, an increasing unit Reynolds number leads to a decreasing slope $h_{II,1}$ (Table 3).

3.2 Analysis of the pressure gradient and unit Reynolds number influence on the transition Reynolds number for gap configurations

In parallel to the above analysis of the reference configuration, the same analysis was carried out for the modified *PaLASTra* model with installed gaps. The fitted linear approximation of the transition Reynolds number as a function of H_{12} is shown as solid lines in Fig. 8 for the considered case at $M = 0.35$ and $Re_1^* = 17.5$, while the middle figures in Appendix (Figs. 22, 25, 28, 31, 34, 37, 40, 43, 46, 49, 52, 55, 58) report the results for the other flow conditions examined in this work. The black dashed lines show the averaged result of the reference configurations, based on the analysis described above (Sect. 3.1). The purple dotted line marks the Reynolds number corresponding to the location of the gap at $x_G/c = 0.35$ with $Re_{x_G} = x_G \cdot Re_1$.

It can be seen that the transition occurs in most analysed cases between the gap and the transition location measured with the reference configuration. As shown also in Fig. 4, a gap of $w = 30 \mu\text{m}$ leads to a reduced transition Reynolds number compared to the reference configuration. A further increase of the gap width to $w = 100 \mu\text{m}$ leads to a further reduction of the transition Reynolds number. However, when the gap width is increased even further to $w = 200 \mu\text{m}$, the transition Reynolds number changes only slightly and corresponds, within the measurement uncertainty, to the transition Reynolds number determined with a gap of $w = 100 \mu\text{m}$. In the case of Fig. 8 this effect is rather small, but it can be clearly seen in the middle figures in Appendix (Figs. 22, 28, 31, 34, 43, 49, 55, 58)

In general, it was also found for the configuration with gaps that an increasing unit Reynolds number leads to an increasing transition Reynolds number (Fig. 60 and Tables 4, 5 and 6) and an increasing unit Reynolds number leads to a decreasing slope (Fig. 61 and Tables 7, 8 and 9). These observations are presented in more detail in Appendix.

4 Results of the transition Reynolds number analysis

The approximated linear functions described above were used to calculate the transition Reynolds numbers at specific values of shape factors $H_{12} = 2.30, 2.40$ and 2.50 , as shown in Fig. 9 with their legend in Fig. 10. The black symbols represent the transition Reynolds numbers measured with the reference configuration. The blue, green and red symbols indicate the transition Reynolds numbers measured with gap widths of $30\ \mu\text{m}$, $100\ \mu\text{m}$ and $200\ \mu\text{m}$, respectively. For comparison, the purple dots mark the flow length Reynolds number of the gap location at $x_G/c = 0.35$. It should be stressed that the shape factors and transition Reynolds numbers shown in Fig. 9 were not measured directly but calculated based on the linear approximations. This approach is very helpful to understand general trends, as presented in the following.

It can be seen from Fig. 9 that the variation of Re_{tr}^* is larger at smaller H_{12} . This effect is caused by the stronger acceleration of the boundary layer (compare Fig. 2 with Fig. 3). It results in a weaker amplification of the T-S waves at smaller H_{12} , which can be observed by comparing the gradients of the N -factor curves (Figs. 5 and 6). A stronger pressure gradient reduces the slope of the N -factor curves and results in a larger difference between the transition locations. This so-called ‘sensitivity effect’ has been described before in detail for forward facing steps in Costantini et al. (2015b, 2016); Costantini (2016) and will be discussed for gaps in Sect. 7.3.

The overview graphs in Fig. 9 also show a reduction of the transition Reynolds numbers by installation of the gaps with widths up to $w = 100\ \mu\text{m}$, provided that the other parameters are kept fixed. However, increasing the gap width from $w = 100\ \mu\text{m}$ to $w = 200\ \mu\text{m}$ does not lead, in general, to a further reduction in Re_{tr}^* , as described in Sect. 3.2. It should be emphasized here that transition occurred generally downstream of the gap even with the largest gaps installed.

4.1 The unit Reynolds number effect

As described above, the transition Reynolds number increases with increasing unit Reynolds number. This observation is known as ‘unit Reynolds number effect’ and has been investigated and discussed in detail in Risius et al. (2018b). It is known that a power relation exists with $Re_{tr}^* \sim (Re_1^*)^{\alpha_{III}}$. The exponents of the results presented here can be found by estimating the slopes of $\log(Re_{tr}^*)$ against $\log(Re_1)$ as done for example for $H_{12} = 2.40$ in Fig. 11. The exponent α_{III} was found to vary between approximately 0.4 and 0.62. It is therefore in agreement

with earlier findings, which are in the same range (Arnal 1989; Risius et al. 2018b).

4.2 Mach number influence

A comparison of the different Mach numbers (data points with same colour and different symbols in Fig. 9) shows that M does not have a systematic influence on Re_{tr}^* outside the measurement uncertainty for the investigated configurations. It should be remarked here that a variation of the Mach number in KRG also leads to a change in the disturbance environment and in the model surface temperature ratio (wall temperature/adiabatic-wall temperature). An exclusive analysis of Mach number effects can be carried out when disturbance levels of the wind tunnel and the wall temperature ratio are taken into account and their influence is corrected, as discussed in Risius et al. (2018b) and in Sect. 6.3.

4.3 Relative change of the transition location

The transition location can also be used to calculate the relative variation of the transition location by the ξ -parameter (see for example Perraud and Séraudie (2000) and Costantini et al. (2015b) for the analysis of step effects, or Crouch et al. (2022) for the study of gaps). The ξ -parameter gives the distance from the gap to the transition location, normalized by this distance in the absence of a gap:

$$\xi = \frac{x_T - x_G}{x_{T0} - x_G} \quad (1)$$

The transition location in the absence of a gap is given by x_{T0} , and in the presence of a gap by x_T , while the location of the gap is fixed at $x_G = 70\ \text{mm}$. For values of $\xi = 1$, the transition position is equivalent to that of the reference configuration, while for values $\xi = 0$, transition occurs directly at the gap.

4.4 Influence of the gap width

In Fig. 12 the ξ -parameter is plotted as a function of the gap width, w , normalized by the boundary layer displacement thickness at the gap location, δ_1 (computed by means of *COCO* for the gap configuration, but assuming that the gap does not exist). It can be seen that a relative increase in gap width compared to boundary layer thickness w/δ_1 leads to a larger reduction of ξ , as expected from the results presented in the previous sections. Small gaps of $w = 30\ \mu\text{m}$ (blue) have a smaller effect than larger gaps with $w = 100\ \mu\text{m}$ (green) or $w = 200\ \mu\text{m}$ (red). A gap width of $w = 30\ \mu\text{m}$ leads to a reduction of the laminar flow length of at least 20 %.

As discussed above, an increase in gap width from $w = 100 \mu\text{m}$ to $w = 200 \mu\text{m}$ does not lead to a further decrease in laminar flow length, i.e. ξ remains practically unchanged for the same flow conditions, although w/δ_1 doubles. Therefore, the green and the red data points do not collapse onto each other. The data points for the $w = 200 \mu\text{m}$ gap configuration are offset by an almost uniform value of $\Delta w/\delta_1 \approx 1$ with respect to the data points of the $w = 100 \mu\text{m}$ gap configuration. For a fixed value of w/δ_1 , the difference between the results of $w = 100 \mu\text{m}$ and $w = 200 \mu\text{m}$ is in the range of $\Delta\xi \approx 20\%$ to 30% . This difference may be caused by different T-S waves leading to different transition locations, as suggested by Zahn and Rist (2015).

It is also remarkable that the gap widths of $w = 100 \mu\text{m}$ and $w = 200 \mu\text{m}$ exhibit an almost linear behavior of ξ as a function of w/δ_1 . The linear trends of $w = 100 \mu\text{m}$ and $w = 200 \mu\text{m}$ are consistent with the determined ξ -values of the $w = 30 \mu\text{m}$ gap.

In agreement with the results described above the Mach number M does not have an appreciable influence on ξ in the investigated parameter range.

4.5 Influence of the shape factor H_{12}

Thanks to the systematic variation of the pressure gradient and the linear approximation of the results the present study allows to investigate ξ for different values of the shape factor H_{12} . The trends and ranges of ξ remain similar for different shape factors $H_{12} = 2.30, 2.40$ and 2.50 (Figs. 14 and 15). These results also show that a decreasing value of H_{12} (stronger favourable pressure gradient) leads to a slight decrease in ξ . The gradient $\Delta\xi/\Delta H_{12}$ was found to be in the range of $\Delta\xi/\Delta H_{12} \approx 0.2$ to 0.65 when H_{12} is varied from $H_{12} = 2.30$ to 2.50 . This effect appears to be small but systematic for all data points and may be related to a remaining ‘sensitivity effect’ in the presence of gaps, such as that described above and in Sect. 7.3.

4.6 Influence of the gap-width Reynolds number Re_w

The same trends as discussed above can be found by plotting ξ over the gap-width Reynolds number Re_w for various values of shape factors $H_{12} = 2.30, 2.40$ and 2.50 , as shown in Figs. 13 and 15. The described offset between the gap width of $w = 100 \mu\text{m}$ and $w = 200 \mu\text{m}$ for the same ξ is in the range of $\Delta Re_w \approx 2500$. For a constant value of Re_w , the offset between gaps with $w = 100 \mu\text{m}$ and $w = 200 \mu\text{m}$ is in the range of $\Delta\xi \approx 20\%$, which is smaller than the variation of $\Delta\xi$ at a constant w/δ_1 (Sect. 4.4).

5 Results of the N -factor analysis

As described in Sect. 2.5 the critical incompressible N -factors were determined by combining the measured transition location with the envelope N -factor curve. The critical N -factors are shown as a function of H_{12} for individual combinations of M and Re_1^* in Fig. 16 and in the bottom figures in Appendix (Figs. 23, 26, 29, 32, 35, 38, 41, 44, 47, 50, 53, 56, 59). The good repeatability of the results from different wind tunnel entries can be seen also by comparing the N -factor results of different reference configurations in these figures.

As introduced in Sect. 2.5, the incompressible critical N -factor is used for the current analysis, since it exhibits better correlations when external disturbance spectra are not corrected (Risius et al. 2018b). The incompressible N -factor is especially useful since we focus on the influence of two-dimensional disturbances on boundary layer transition, and not on the influence of environmental disturbances. Nevertheless, a similar analysis was carried out for compressible critical N -factors, leading to similar results as shown here (not included).

5.1 Mach number influence

The influence of the Mach number, M , on the relative reduction of the N -factor, ΔN , is investigated explicitly in Fig. 17. It can be seen that the Mach number has no systematic influence on the relative reduction of the critical N -factor, at least in the examined Mach number range. This result is in agreement with the findings reported in Sect. 4, in which no appreciable influence of the Mach number on transition Reynolds number and on ξ was observed.

5.2 Influence of the shape factor H_{12}

The shown N -factor distributions exhibit a plateau for decelerated boundary layers with $H_{12} > 2.60$. For accelerated and neutral boundary layers with $H_{12} \lesssim 2.60$ the critical N -factors decrease almost linearly with shape factor H_{12} . This finding is in agreement with the results reported in Risius et al. (2018b), and a further discussion of this effect is carried out in Sect. 7.3. It is shown in Fig. 16 and in the bottom figures in Appendix (Figs. 23, 26, 29, 32, 35, 38, 41, 44, 47, 50, 53, 56, 59) that the influence of the pressure gradient on the critical N -factors is similar for all gap configurations as on the reference configuration for $H_{12} \lesssim 2.60$. In the following analysis we focus on the favourable and nearly zero

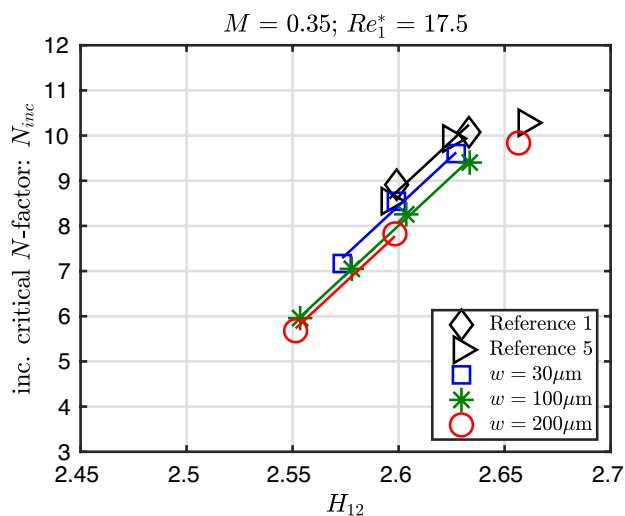


Fig. 16 Critical N -factors as a function of H_{12} for different reference configurations and gap widths. The flow conditions are $M = 0.35$ and $Re_1^* = 17.5$. The flow conditions are the same as in Figs. 7 and 8

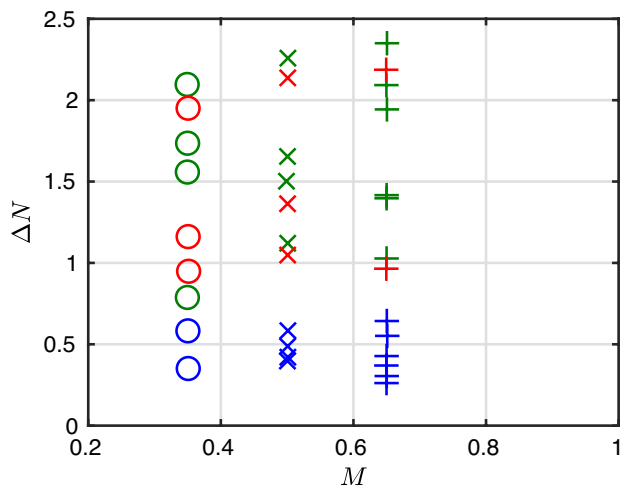


Fig. 17 Relative reduction of the critical N -factor, ΔN , caused by the gap, plotted as a function of Mach number M . The legend is shown separately in Fig. 10

pressure gradients, which shows a linear behaviour and is most relevant for NLF airfoils.

5.3 Influence of the gap width

In agreement with the results of the transition Reynolds number (Sect. 4), the N -factor is reduced by the installation of gaps compared to the reference configuration (bottom figures in Appendix, i.e. Figures 23, 26, 29, 32, 35, 38, 41, 44, 47, 50, 53, 56, 59). The graphs show a significant reduction of the critical N -factor for $w = 30 \mu\text{m}$ and a further reduction for gaps with $w = 100 \mu\text{m}$, but no further decrease if the gap width is extended to $w = 200 \mu\text{m}$. This behavior is obviously

related to that of the transition Reynolds number as a function of the gap width, discussed above.

In order to determine the reduction of the critical N -factor by installation of the gap, a linear function is used to approximate the dependency of the incompressible critical N -factor on H_{12} . This approximation is carried out separately for each gap width and for each flow condition, defined by the specific M and Re_1^* . For each dataset the range of H_{12} used for the linear approximation was chosen separately depending on the distribution of the data points used. In fact, due to the scatter of the data, it was not possible to define a universal range of H_{12} that allows a useful linear approximation for all test conditions. Instead, the range of the plateau and the range of the linear approximation slightly varied for each test condition.

The analysis of the different N -factor distributions shows that, despite the change of N as a function of H_{12} for $H_{12} \lesssim 2.60$, the gap-induced ΔN remains essentially uniform. Thus, a uniform $\Delta N = N_{\text{reference}} - N_{\text{gap}}$ is assumed. In order to quantify the constant offset by ΔN the determined slopes for all configurations were averaged and plotted for the approximated range of H_{12} : they are presented as solid lines with the colours of the corresponding datasets in the bottom figures in Appendix (Figs. 23, 26, 29, 32, 35, 38, 41, 44, 47, 50, 53, 56, 59). By comparing the offset between the linear approximations, the resulting reductions of the critical N -factors, caused by the installation of the gaps, are determined systematically and compared. It should be recalled here that the analysis focuses on the favourable and zero pressure gradients, while adverse pressure gradients are not considered, as mentioned in Sect. 5.2 and discussed also in Sect. 7.3.

The change of the critical N -factor, ΔN , is shown as a function of the relative gap width w/δ_1 in Fig. 18. It shows that an increasing gap width generally leads to an increasing ΔN . Since the reduction of critical N -factors of $100 \mu\text{m}$ and $200 \mu\text{m}$ is similar although the gap width is doubled, the data points for $200 \mu\text{m}$ lay at larger w/δ_1 for approximately the same ΔN . Figures 17 and 18 show that a gap width of $w = 30 \mu\text{m}$ reduces the critical N -factors in the range of $\Delta N \approx 0.5 \pm 0.25$, while gap widths of $w = 100 \mu\text{m}$ and $w = 200 \mu\text{m}$ reduce the critical N -factor in the range of $\Delta N \approx 1.5 \pm 1$.

The obtained data can be used to estimate a worst case and a best case scenario for the influence of the considered gaps on the critical N -factors. To estimate the bounding limits of the critical N -factor change, limiting linear functions are drawn through the origin in Fig. 18. The estimated worst case limit, which gives the largest influence of the gap on ΔN , is approximated to be $\Delta N \approx 1.5 \cdot w/\delta_1$, which is shown by a red dashed line in Fig. 18. The best case scenario, which gives the smallest influence that a gap has on ΔN , is given by $\Delta N \approx 0.4 \cdot w/\delta_1$ (blue dotted line in Fig. 18). The average

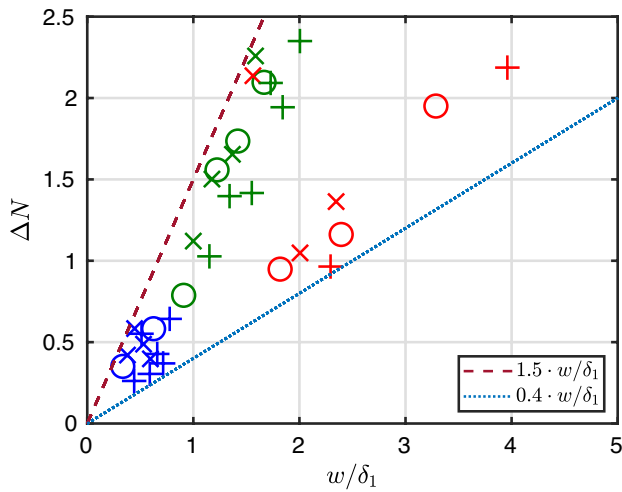


Fig. 18 Reduction of the critical N -factor caused by the gap, ΔN , plotted against normalized gap width, w/δ_1 . Worst case and best case scenarios are indicated by a red dashed and a blue dotted line, respectively. The further legend is shown separately in Fig. 10

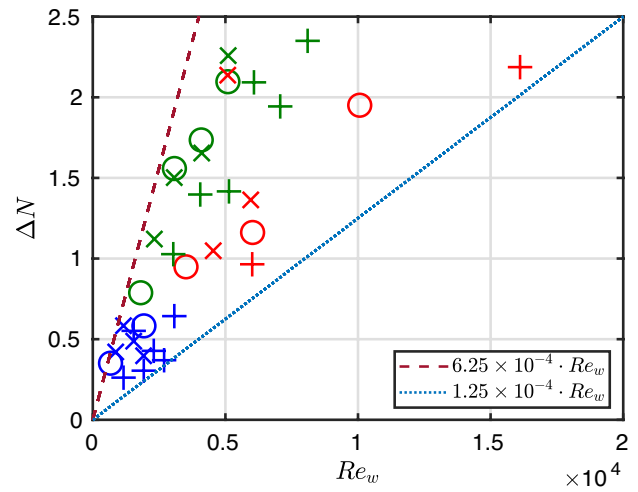


Fig. 19 Reduction of the critical N -factor caused by the gap, ΔN , plotted as a function of gap-width Reynolds number, Re_w . Worst case and best case scenarios are indicated by a red dashed and a blue dotted line, respectively. The legend is shown separately in Fig. 10

slope of these two extreme values is 0.95, which may be used as a rule of thumb to estimate the expected reduction of the critical N -factor. In practice, a gap with the width of the displacement thickness at the gap location would lead to a reduction of the critical N -factor of $\Delta N \approx 1$.

The values of ΔN found in the present work are within the range of critical N -factor changes reported by Crouch (2022) and Crouch et al. (2022) for deep gaps not causing bypass transition. However, the observed change in critical N -factor is about ten times larger than that reported for deep gaps by Crouch (2022) and Crouch et al. (2022) ($\Delta N = 0.1 \cdot w/\delta_1$). These aspects will be further discussed in Sect. 7.4.

5.4 Influence of the gap-width Reynolds number

An analysis similar to that of Fig. 18 can be performed with ΔN as a function of the gap-width Reynolds number, Re_w , as shown in Fig. 19. The discrepancy between the datasets with $w = 100 \mu\text{m}$ and $w = 200 \mu\text{m}$ can also be seen in this case. The worst case scenario is estimated to be

$$\Delta N \approx 6.25 \times 10^{-4} \cdot Re_w \text{ (red dashed line)}$$

and the best case scenario is estimated to be

$$\Delta N \approx 1.25 \times 10^{-4} \cdot Re_w$$

(blue dotted line in Fig. 19). The expected increase of ΔN , calculated as the average slope of these two extreme values, is given by $\Delta N = 3.75 \times 10^{-4} \cdot Re_w$.

6 Repeatability of the data and uncertainties in the results

6.1 Repeatability of wind tunnel entries

As described in Sect. 3, the measurements were conducted over a time span of two years in six different measurement campaigns. During this period the model was reassembled several times and the reference configuration was repeatedly tested in each wind tunnel entry. The good repeatability of the data can be seen by comparing the reference data of different measurement campaigns (Figs. 7, 21, 24, 27, 30, 33, 36, 39, 42, 45, 48). The same good repeatability was observed for the configuration with $w = 100 \mu\text{m}$ (Fig. 40).

6.2 Turbulent flow features

A significant source of uncertainty in the current study may be found in the transition location detected in some model areas, especially at large Reynolds numbers and large gap sizes. Although the TSP measurement technique and the method of transition detection are very reliable and lead to very accurate and repeatable results (Costantini et al. 2021), the effect of turbulent wedges and other turbulent flow features has to be taken into account. This effect becomes increasingly important with increasing Reynolds number, i.e. with decreasing boundary layer thickness, since the relative size of dust particles or other sources of contamination increases with respect to δ_1 , and these disturbances are more likely to cause earlier transition to turbulence. As described in Sect. 2.1, turbulent wedges and side wall effects were excluded from the analysis for the

detection of the transition location. However, the question arises which other flow features are to be in- or excluded from the range of transition detection. An example for it can be seen in the last result of Fig. 4. In this result, side wall effects and the turbulent wedge in the mid-span area were excluded from the transition detection region, but a small area with transition slightly upstream of the average transition location was included (see red dots in the figure). Since it is not possible to identify objectively in all cases which areas are to be included in the analysis, decisions have to be made individually for each image. This customary decision process leads to some small uncertainties; nevertheless, averaging over the complete span reduces the specific weight of the individual decision. Furthermore, the conservative uncertainty estimation of the transition Reynolds number incorporates these uncertainties, as discussed in the next section.

6.3 Uncertainties of measured parameters

Risius et al. (2018b) reported uncertainties of the transition Reynolds number and of the pressure gradient parameter that are in the range of $(Re_{tr}^*)_{RMS} \approx 0.5$ and $(H_{12})_{RMS} \approx 0.01$, which correspond to relative errors of about 5% and 0.5%, respectively. The conservative estimation of $(Re_{tr}^*)_{RMS} \approx 0.5$ from previous work is considered in the current analysis, in order to take into account also the uncertainty in the transition detection due to the turbulent flow features (see previous section). The maximal relative uncertainty of ξ can be estimated to be about 7%, which also corresponds to an absolute maximal error of $\Delta\xi \approx 0.07$. The maximal uncertainty in the pressure gradient parameter of $(H_{12})_{RMS} \approx 0.01$ from Risius et al. (2018b) holds also for the current analysis.

An exception for the conservative estimation of $(Re_{tr}^*)_{RMS} \approx 0.5$ can be observed in the image of the reference configuration (very left in Fig. 4) where the transition location is very close to the end of the TSP coated area (which is at $x/c \approx 97.5\%$). The detection of the transition location has in this case a larger uncertainty (in the range of $(Re_{tr}^*)_{RMS} \approx 1$).

6.4 Uncertainties in the critical N -factor analysis

The quantification of the uncertainty of the critical N -factor is difficult as it requires to make assumptions about the receptivity process and the appropriateness of the linear stability analysis. However, when the conservative uncertainty estimation of the transition location is projected onto the N -factor curve, a maximal uncertainty of $N \approx \pm 1$ can be estimated, based on a similar analysis in Risius et al. (2018b).

In order to determine the reduction of the critical N -factor by installation of the gaps, ΔN , a linear function is fitted at certain ranges of H_{12} to the critical N -factor distribution

(see Sect. 5). Accordingly, the uncertainty of ΔN can also be estimated to be in the range of $\Delta N \approx \pm 1$.

7 Discussion

In this section, the influence on the transition Reynolds number and critical N -factor of the examined parameters, i.e. unit Reynolds number (Sect. 7.1), Mach number (Sect. 7.2), pressure gradient (Sect. 7.3) and gap width (Sect. 7.4), as investigated systematically in this study, is summarized and discussed. In Sect. 7.5 the possible influence of an organ-pipe mechanism on laminar–turbulent transition, as described by Zahn and Rist (2015), is discussed with respect to the current results.

7.1 Unit Reynolds number influence

The influence of the unit Reynolds number, Re_1 , on the transition Reynolds number, Re_{tr} , and the critical N -factor is reported in detail in Risius et al. (2018b) for the reference configuration. The general trend of an increasing Re_{tr} with increasing Re_1 was also found in the current investigation for all configurations with and without gaps (see Fig. 9).

A clear dependency of the critical N -factor on Re_1 was not found, neither for the reference configuration nor for the gap configurations. This result is also in agreement with the observations reported in Risius et al. (2018b) for the reference configuration. It should be stressed here that the investigated Reynolds number range between $Re_1 = 17.5 \times 10^6$ and 80×10^6 is significantly larger than those examined in previous studies on the influence of gaps, where $Re_1 < 5 \times 10^6$, as discussed in Sect. 1. It is the first time that the effect of the variation of such a high Re_1 on gap-induced transition has been investigated.

7.2 Mach number influence

The current study is a systematic experimental investigation of gap effects on the transition Reynolds number and the critical N -factor for three different subsonic Mach numbers, $M = 0.35$, 0.50 and 0.65 . For the present experimental setup, it was found that the Mach number has neither an appreciable influence on the measured Re_{tr} nor on ΔN . A recent overview over studies carried out by ONERA is given by Beguet et al. (2017). All these studies were conducted in low-speed environment with significantly smaller Mach numbers ($M < 0.3$). Only Zahn and Rist (2015) have investigated the influence of gaps on laminar–turbulent transition (numerically) at a higher

Mach number ($M = 0.6$), but they have not investigated the influence of different flow speeds. Therefore, the current study is also the first systematic investigation of the Mach number influence on gap-induced transition.

In this context it is important to note that in KRG the intensity of the total pressure fluctuations increases with M (Koch 2004; Risius et al. 2018b). In order to isolate Mach number (i.e. compressibility) effects from effects due to the disturbance level of the wind tunnel and to the wall temperature ratio, a systematic analysis of these additional effects is required, such as the one described in Risius et al. (2018b). In the current study, this kind of systematic correction has not been conducted, as it requires a large number of data points for each model configuration and a detailed knowledge of the disturbance environment. The latter would require details on the receptivity process in the presence of gaps, which are unknown and will result in further uncertainties. In this study, the data are therefore presented directly as a function of Mach number, and the complex analysis for the isolation of the compressibility effects is outside the scope of the current work.

7.3 Influence of the pressure gradient

The influence of the pressure gradient was investigated with help of the incompressible shape factor $H_{12} = \delta_1/\delta_2$. A smaller shape factor leads to a weaker amplification of the T-S waves, which results in larger laminar flow lengths and higher transition Reynolds numbers. The described effect leads to the negative slopes in Tables 3, 7, 8 and 9 and the corresponding Figs. 7, 8 and the top and middle figures in Appendix.

With a stronger favourable pressure gradient, the influence of the gap leads to larger differences in the transition Reynolds number. This effect can be seen in the figures mentioned above or in Fig. 9 by comparing the results for different values of H_{12} . It is consistent with linear stability theory coupled with the e^N method: a stronger favourable pressure gradient leads to a slower growth of T-S waves and the relative influence of the gap is larger at smaller values of H_{12} because the relative change of the laminar flow length is larger. It can be explained in detail by comparing the pressure distributions in Figs. 2 and 3 and the corresponding N -factor distributions in Figs. 5 and 6. Assuming that the critical N -factor remains the same, the relative reduction in laminar flow length due to the effect of the gaps is less pronounced for a steeper N -factor curve (larger H_{12} , see Fig. 5) than for a case with stronger flow acceleration (Fig. 6). This so-called ‘sensitivity effect’ has been explained and discussed before in detail for forward facing steps in Costantini et al. (2015b, 2016), Costantini (2016).

The influence of H_{12} on the N -factor is shown in Fig. 16 and the bottom figures in Appendix. It was found that H_{12} has a non-negligible influence on the N -factor for an accelerated boundary layer. Only at larger values of the shape factor ($H_{12} > 2.60$) corresponding to decelerated boundary layers, the critical N -factors were found to reach a plateau. The dependency of the critical N -factor on H_{12} was already mentioned by Arnal et al. (1997) and was accounted to shortcomings of the e^N -method as for instance, non-parallel effects, the receptivity process or nonlinear mechanisms (Risius et al. 2018b).

In the current investigation the critical N -factor was assumed to be linearly dependent on H_{12} , which was found to be a good approximation for $H_{12} \lesssim 2.60$. Based on this approximation it is also possible to calculate the offset in the critical N -factors by different configurations: $\Delta N = N_{\text{reference}} - N_{\text{gap}}$ (see Sect. 5.3). In the decelerated region with $H_{12} \gtrsim 2.60$ the influence of the gap on the N -factor cannot be quantified in terms of ΔN as the critical N -factor reaches a common plateau region (see for example Figs. 32 and 44). Instead the critical N -factor appears to be dominated by the adverse pressure gradient, while the influence of the gap seems negligible in these cases.

The only other study where the influence of gaps on laminar–turbulent transition has been investigated for different pressure gradients is Crouch et al. (2022). The pressure gradient in their study was however not uniform. For favourable and zero pressure gradients, which are the main focus of the present work, the ΔN model is confirmed to be very effective for predicting the gap-induced changes in transition with predominant T-S waves. However, the present findings for the examined adverse pressure gradients suggest to conduct a dedicated investigation to evaluate in more detail the applicability of the ΔN model for decelerated boundary layers at the examined conditions.

7.4 Influence of gap widths

The influence of gaps on the transition location is investigated by the transition Reynolds number and the ξ -parameter, which gives the relative change in transition location with the installed gap (x_T) compared to the reference configuration (x_{T0}) and the gap location (x_G): $\xi = (x_T - x_G)/(x_{T0} - x_G)$.

As expected, an increasing normalized gap width w/δ_1 leads to an increasing reduction of the laminar flow length, corresponding to a smaller Re_{tr} (Fig. 9) and smaller ξ (Figs. 12 and 13). These trends are in agreement with findings by Beguet et al. (2017), Crouch (2022) and Crouch et al. (2022), who considered shallower gaps. In order to categorize their findings Beguet et al. (2017) map their results onto a width-depth plane with four quadrants depending on the width, w/δ_1 , and the depth, d/δ_1 , of the gap normalized by

the displacement thickness. For values with $w/\delta_1 > 18$ and $d/\delta_1 > 2$ transition has been found to be triggered at the gap location, potentially as a result of some form of bypass mechanism (Beguet et al. 2017; Crouch 2022; Crouch et al. 2022). The results of the current study with $w/\delta_1 \lesssim 4 \ll 18$ and $d/\delta_1 \gtrsim 80 \gg 2$ are located in the ‘high top left’ quadrant of the width-depth plane, which seems to be practically unexplored.

Accordingly to the findings discussed in this work the critical N -factor is reduced and ΔN increases almost linearly with w/δ_1 (Fig. 18) and with Re_w (Fig. 19). These findings are in agreement with the general trends as reported by Crouch (2022), Crouch et al. (2022) and also the values of $\Delta N \approx 0.2$ to 2.5 are in the same ranges (when no bypass transition occurs). The minimal and maximal change in ΔN can be approximated linearly and used to predict the influence of gaps for other flow conditions (see Sect. 5.3 and Sect. 5.4). The reduction of the critical N -factor can be approximated to be in average of the order of $\Delta N = 0.95 \cdot w/\delta_1$ or $\Delta N = 3.75 \times 10^{-4} \cdot Re_w$. The worst case limit was found to be $\Delta N = 1.5 \cdot w/\delta_1$ in this study. These gradients of the linear approximation of ΔN vs. w/δ_1 are about a factor ten larger than the slopes of $\Delta N = 0.122 \cdot w/\delta_1$ for deep gaps reported by Crouch (2022); Crouch et al. (2022). This difference may be related to both the depth of the gaps (which are much deeper than the gaps investigated by Crouch (2022); Crouch et al. (2022)) and the larger Mach numbers, which were not considered in their model. Moreover, the pressure gradient effect was also not studied systematically by Crouch (2022); Crouch et al. (2022). Furthermore, as mentioned above, we are in the ‘high top left’ quadrant of the width-depth plane, which has not been explored before. All these aspects may be a possible cause for the observed discrepancies. Another cause leading to the observed discrepancy may be the secondary T-S waves emitted by the gap, as discussed below.

7.5 The organ-pipe mechanism inside the gap

An important observation of the current study is the fact that a further upstream shift in transition location is not observed when the gap width is doubled from $w = 100 \mu\text{m}$ to $w = 200 \mu\text{m}$. For both cases the measured transition locations are almost identical, despite the significantly larger values of w/δ_1 and Re_w for the $200 \mu\text{m}$ case. This observation and the other results described above may be explained by the organ-pipe mechanism investigated by Zahn and Rist (2015).

The flow conditions in the current investigation are comparable to the flow condition of the study by Zahn and Rist (2015). In their study the width is $w \approx 640 \mu\text{m}$, which is comparable to the boundary-layer thickness in their case. It leads to a gap width Reynolds number of $Re_w = 8800$ and

a gap depth Reynolds number ranging from $Re_d \approx 48 \times 10^3$ to $Re_d \approx 333 \times 10^3$. In their simulation the boundary-layer flow above the gap is only slightly influenced by the gap, while in the gap itself a recirculation region is established. They found a remarkable influence on the N -factor caused by an organ-pipe mechanism inside the gap, which leads to a resonance effect and a superposition of the original T-S wave with a new T-S wave generated by the gap. Even though these effects could not be tested directly in the current study, the observations by Zahn and Rist (2015) may be helpful to explain the present observations. According to their study the effect of the gap may be divided into two parts. The first part is an enhanced growth of the original T-S waves, caused by a modification of the base flow due to the gap. The second part is due to the aforementioned new T-S wave generated by the gap. While for small gaps with $w \approx 30 \mu\text{m}$ the enhanced growth of the N -factor may be mainly due to the modification of the base flow and thus related to the gap width, it may be different for larger gaps with $w \gtrsim 100 \mu\text{m}$. In this case the transition process may be dominated by the T-S waves generated by the gap, which may remain identical for gap widths of $100 \mu\text{m}$ and $200 \mu\text{m}$.

Zahn and Rist (2015) investigate the influence of gap depth on the T-S wave and show that the parameter d/λ has an influence on the amplification of the T-S wave and therefore also onto the expected transition location. In Fig. 20 the transition Reynolds number is shown as a function of the parameter d/λ . The present observations lead to the presumption that the process of T-S waves-inducing transition for a gap of $30 \mu\text{m}$ is different from the mechanism at larger gap widths with $100 \mu\text{m}$ and $200 \mu\text{m}$.

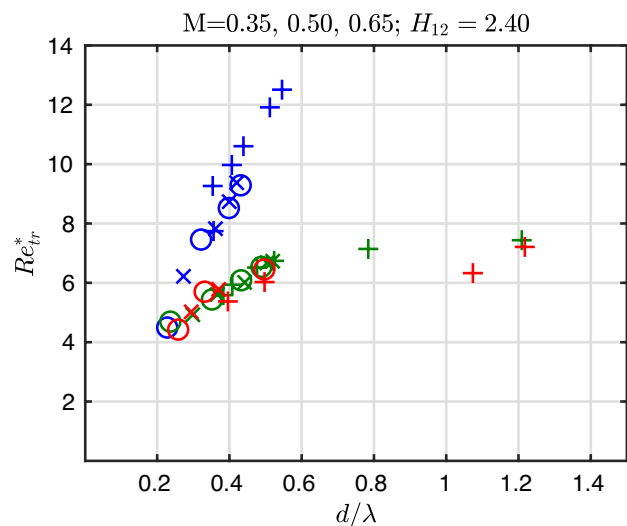


Fig. 20 Transition Reynolds number Re_{tr}^* as a function of gap depth d over T-S wave length λ at $H_{12} = 2.40$. The legend is shown separately in Fig. 10

Another hint to support this consideration might be the deviation of the variables $h_{II,0}$ and $h_{II,1}$ of Eq. II of the 100 μm (Table 8) and 200 μm (Table 9) gaps, as discussed in Appendix.

Zahn and Rist (2015) predict a fluctuating resulting amplitude of the T-S wave with d/λ (Fig. 15 in Zahn and Rist (2015)), which may lead to a fluctuating Re_{tr}^* with d/λ . Such amplitude-induced fluctuation might be present in the results for gap widths of 100 μm and 200 μm in Fig. 20. Unfortunately, the resolution in the range $d/\lambda > 0.6$ is not fine enough to prove the conjectured organ-pipe mechanism.

In order to verify this speculation more research will be needed in the future. The measurement of T-S wave frequencies with hot-films on the model may be a possibility to clarify this question. In any case, it should be emphasized that the variation of ξ and ΔN may still depend on other parameters. The change in the specific flow conditions (in particular δ_1 and Re_1) at fixed w and d leads to the observed change in ξ and ΔN for varied w/δ_1 or Re_w , but at the same flow conditions (with a change in w from 100 μm to 200 μm) transition occurs at the same location (and ξ and ΔN remain the same, although w/δ_1 and Re_w vary). Therefore, it will be needed to investigate the effect of d and w on transition separately in a future investigation.

8 Conclusions

In conclusion we may emphasize that this study shows a systematic investigation of the effects of gaps on transition Reynolds numbers and critical N -factors at various pressure gradients, Mach and Reynolds numbers. The influence of three different gap sizes was investigated at subsonic flow speeds at high Reynolds numbers. The Temperature-Sensitive Paint technique was proven to be reliable for transition detection and the quantitative measurement of the surface temperature. The measured temperature and pressure distributions were used as input for boundary layer calculations and linear stability analysis. By correlation with the measured transition locations, critical N -factors were determined, and the influence of gaps was quantified by the ΔN -method. The transition Reynolds numbers and critical N -factors of six wind tunnel entries of the reference configuration over two years show a very good repeatability of the test results.

The installation of gaps with 30 μm width leads to a reduction of Re_{tr} and critical N -factor. Increasing the gap width from $w = 30 \mu\text{m}$ to 100 μm results in a further reduction of the critical N -factor. However, increasing the gap width to 200 μm did not cause an even further reduction of the transition Reynolds number and the critical N -factor. These results may be explained by an organ-pipe

mechanism inside the gap causing an additional T-S wave to be emitted by the gap, which may interact with the original T-S waves downstream of the gap (Zahn and Rist 2015). For larger gap widths ($w = 100 \mu\text{m}$ and 200 μm), the gap-generated T-S wave may have a dominating influence on the transition location in such a way that the influence of the gap width on the base flow becomes negligible.

The relative reduction of the critical N -factor was investigated as a function of w/δ_1 and Re_w . For each relationship a best case and worst case scenario was approximated by linear functions. These linear relations allow to approximate the expected ΔN as functions of w/δ_1 and Re_w . The estimated worst case influence of the gap was found to be $\Delta N = 1.5 \cdot w/\delta_1$, which can be used as a worst case limit to estimate the effect of the gaps on transition for the examined flow conditions. The variation of ΔN in this case is about ten times larger than the results by Crouch et al. (2022). This discrepancy may be due to the significantly deeper gaps examined in the present work, coupled with the different flow conditions and the possible occurrence of the aforementioned organ-pipe mechanism inside the gap.

By this systematic investigation it was found that the Mach number has neither a significant influence on the transition Reynolds number Re_{tr} nor on the critical N -factor under the described experimental conditions with installed gaps. It was found that Re_{tr} increases with Re_1 , which is known as ‘unit Reynolds number effect.’ The slope α_{III} of the relation $Re_{tr}^* \sim (Re_1^*)^{\alpha_{III}}$ was found to vary between 0.4 and 0.62, in agreement with earlier investigations (Risius et al. 2018b).

The measurement at different pressure gradients allowed to compare the gap influence at different H_{12} . The results show that the relative influence of gaps causes a stronger reduction of Re_{tr} at smaller H_{12} , corresponding to stronger favourable pressure gradients. The trends of ξ at different H_{12} are found to be similar, i.e. H_{12} has no major influence on the ξ -dependency of the non-dimensional gap parameters. However, a larger H_{12} (corresponding to a less pronounced pressure gradient) was found to lead to slightly increasing values of ξ , which may be related to a remaining sensitivity of transition on the pressure gradient in the presence of the gaps.

In summary, the described results can be helpful to design laminar airfoils and define appropriate maximum gap sizes and manufacturing tolerances. Furthermore, the results stress the need to investigate possible resonance effects, as for example the organ-pipe mechanism, and their influence on T-S wave induced laminar–turbulent transition. Such resonance effects may also be helpful to compensate flow disturbances by two-dimensional excrescences and therefore stabilize laminar flow regimes.

Appendix

Appendix consists out of two parts. The first part shows the detailed results for each flow condition in a series of three succeeding images. The first image on top shows the transition Reynolds number of reference configuration at different wind tunnel entries (labelled as Reference 1–6). The individual results of the reference configurations are combined to give a linear reference function shown as dashed black lines in the top figures.

The second images in the middle show also the results of the reference configuration marked with black dashed lines. The purple dotted horizontal line marks the transition Reynolds number which corresponds to the location of the gap at $x_G/c = 0.35$ with $Re_{x_G} = x_G \cdot Re_1$. In the middle between the boundaries given by the reference configuration and the gap location, the measured transition Reynolds numbers of different gap configurations are shown by blue ($w = 30 \mu\text{m}$), green ($w = 100 \mu\text{m}$) and red ($w = 200 \mu\text{m}$) lines.

The last image at the bottom shows the corresponding results of the critical N -factors. In the ranges of H_{12} where a linear increase in the critical N -factor was observed a linear function with an average slope was fitted to the results. The offset between the different linear approximations was used to determine the value of ΔN used for the analysis in Sect. 5.

The second part of Appendix contains Tables 4 to 9 of the fitted linear approximations with intercepts, $h_{II,0}$, and slopes, $h_{II,1}$, of Eq. II for each gap configuration. These results are also summarized in Figs. 60 and 61. In general, it was also found for the configuration with gaps that an increasing unit Reynolds number leads to an increasing transition Reynolds number (Fig. 60 and Tables 4, 5 and 6) and an increasing unit Reynolds number leads to a decreasing slope (Fig. 61 and Tables 7, 8 and 9). An exception to this behavior was found at cases of the largest Mach number ($M = 0.65$) with high Reynolds numbers ($50 \leq Re_1^*$) for gap widths of $w = 100 \mu\text{m}$ and $w = 200 \mu\text{m}$. A possible reason for this abnormal trend may be an organ-pipe mechanism inside the gap which triggers a new T-S wave as described by Zahn and Rist (2015) and discussed in more detail in Sect. 7.4. However, it should be stressed that the observed scattering of the intercept for different Mach numbers at $Re_{tr}^* = 30$, 40 and 50 is approximately $\Delta Re_{tr}^* \approx 20$ and based on a significant extrapolation of the measurement data. Furthermore, the basis for this extrapolation at high Mach and Reynolds numbers is only a few measurement points. It is therefore difficult to make a definite statement based on the observed trends shown in Figs. 60 and 61.

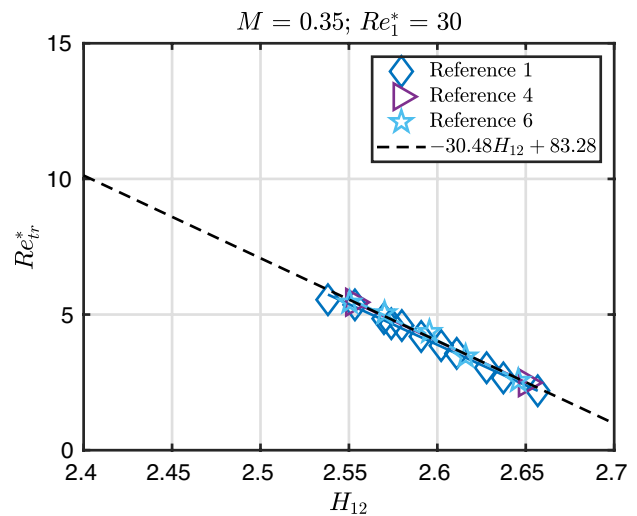


Fig. 21 Re_{tr}^* as a function of H_{12} for the reference configuration

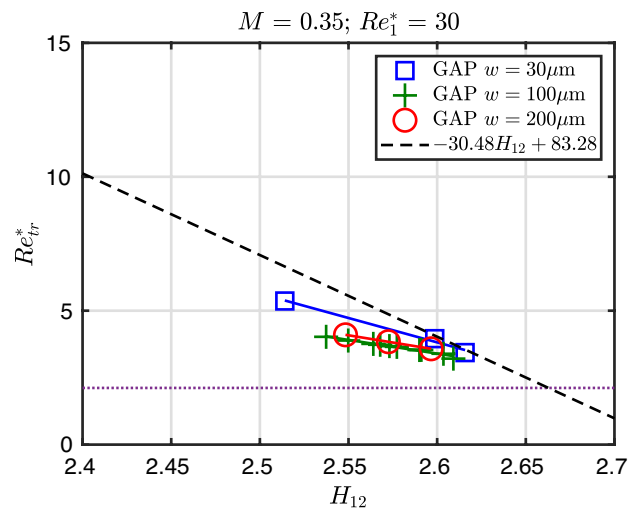


Fig. 22 Re_{tr}^* as a function of H_{12} the configurations with gaps

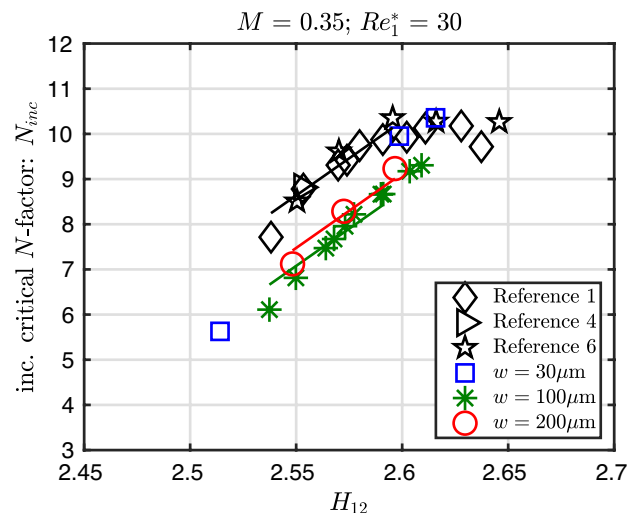


Fig. 23 Inc. critical N -factors as a function of H_{12} for different reference configurations and gap widths with $M = 0.35$, $Re_1^* = 30$

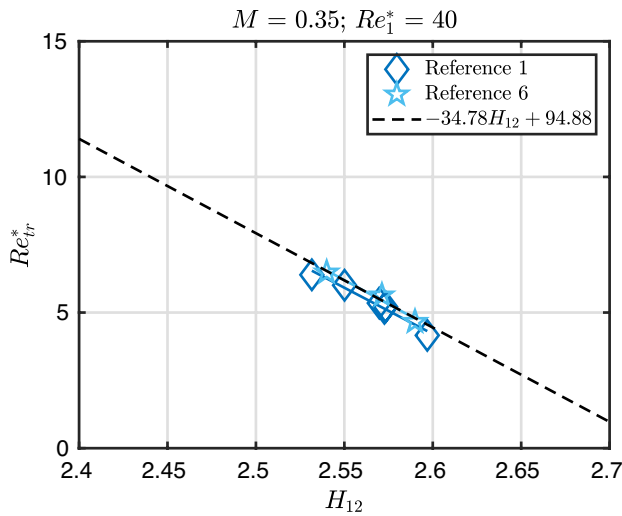


Fig. 24 Re_{tr}^* as a function of H_{12} for the reference configuration

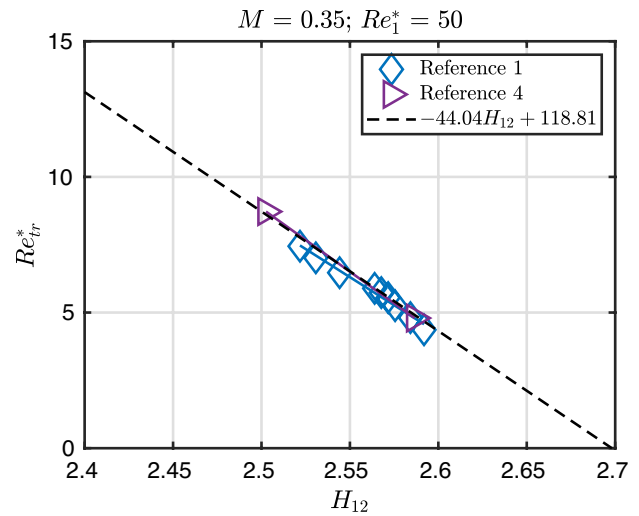


Fig. 27 Re_{tr}^* as a function of H_{12} for the reference configuration

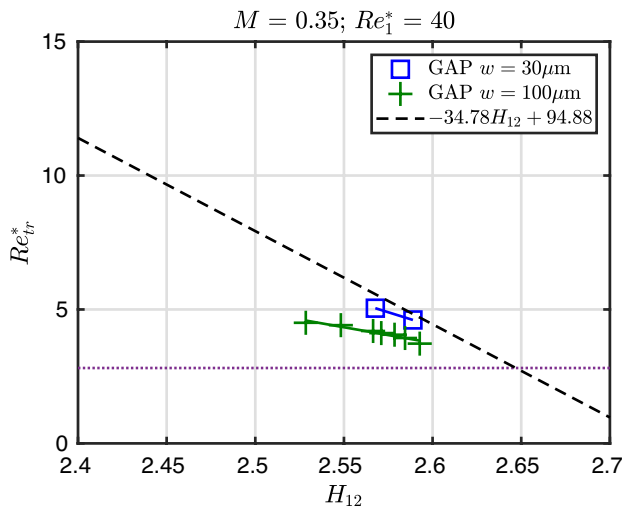


Fig. 25 Re_{tr}^* as a function of H_{12} the configurations with gaps

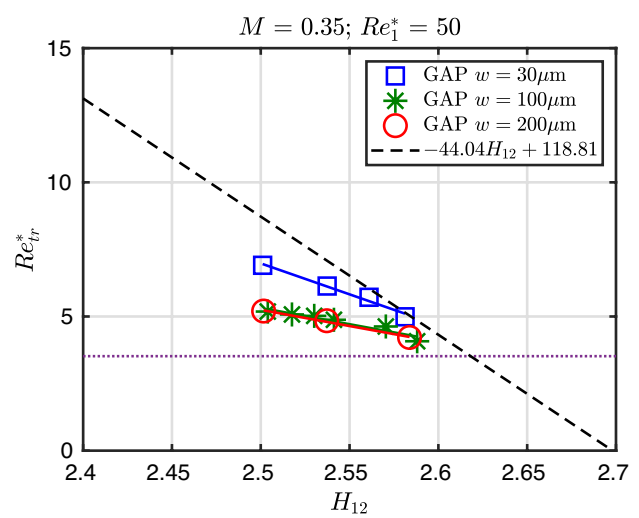


Fig. 28 Re_{tr}^* as a function of H_{12} the configurations with gaps

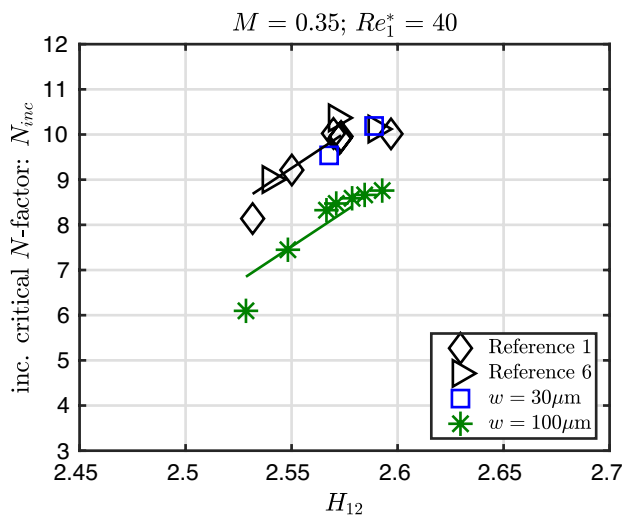


Fig. 26 Inc. critical N -factors as a function of H_{12} for different reference configurations and gap widths with $M = 0.35$, $Re_1^* = 40$

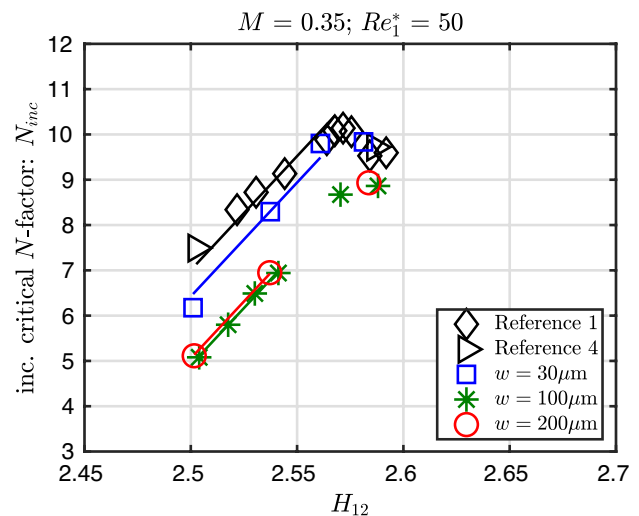


Fig. 29 Inc. critical N -factors as a function of H_{12} for different reference configurations and gap widths with $M = 0.35$, $Re_1^* = 50$

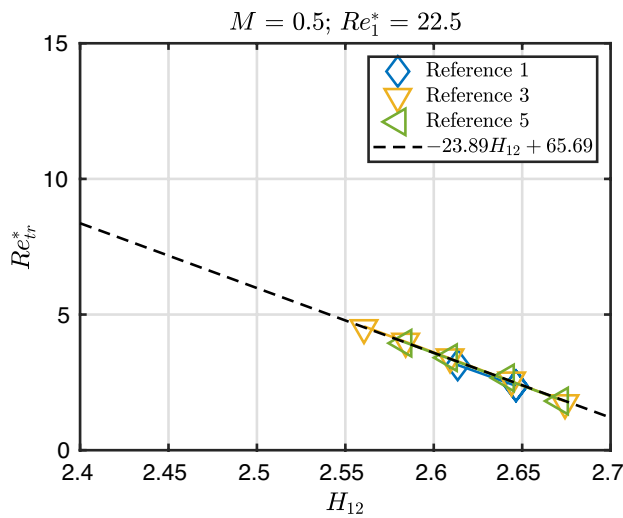


Fig. 30 Re_{tr}^* as a function of H_{12} for the reference configuration

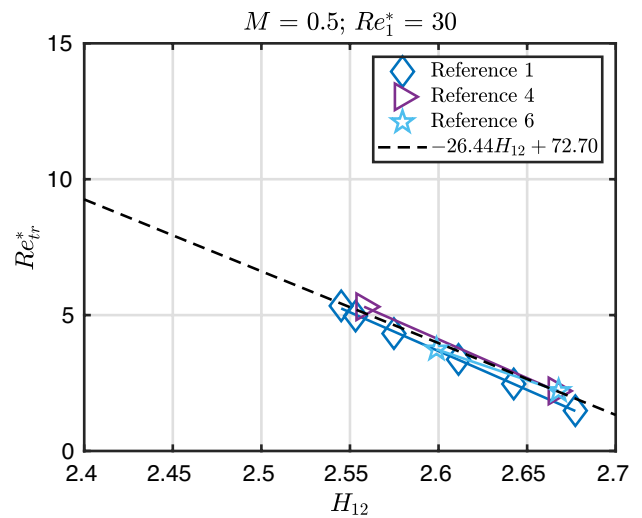


Fig. 33 Re_{tr}^* as a function of H_{12} for the reference configuration

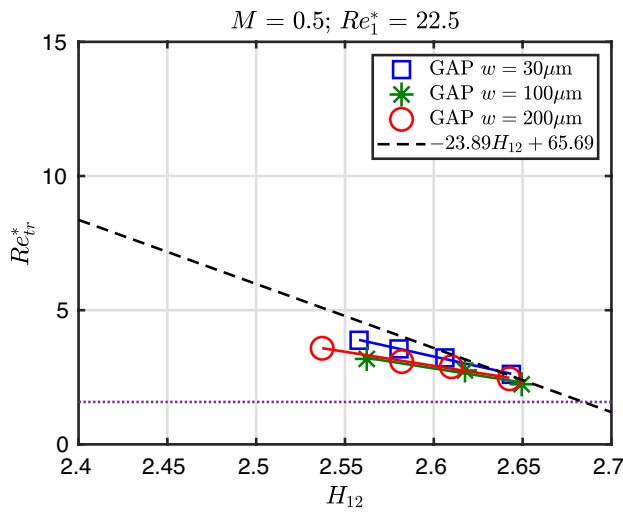


Fig. 31 Re_{tr}^* as a function of H_{12} the configurations with gaps

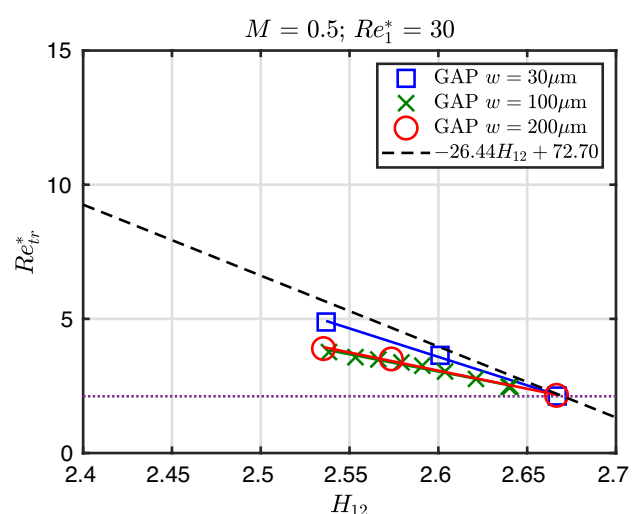


Fig. 34 Re_{tr}^* as a function of H_{12} the configurations with gaps

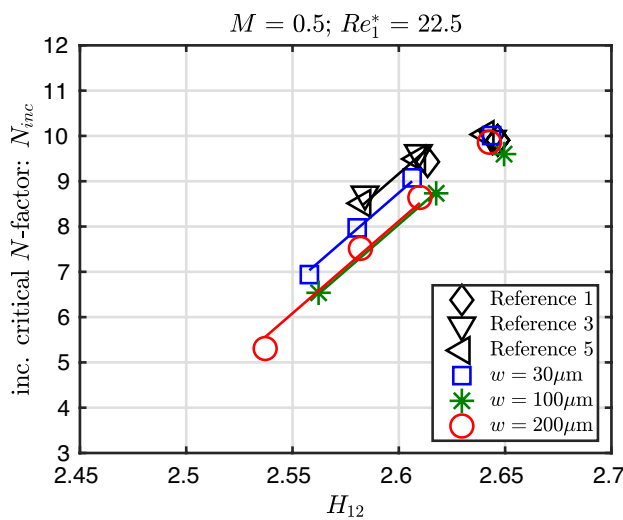


Fig. 32 Inc. critical N -factors as a function of H_{12} for different reference configurations and gap widths with $M = 0.50$, $Re_1^* = 22.5$

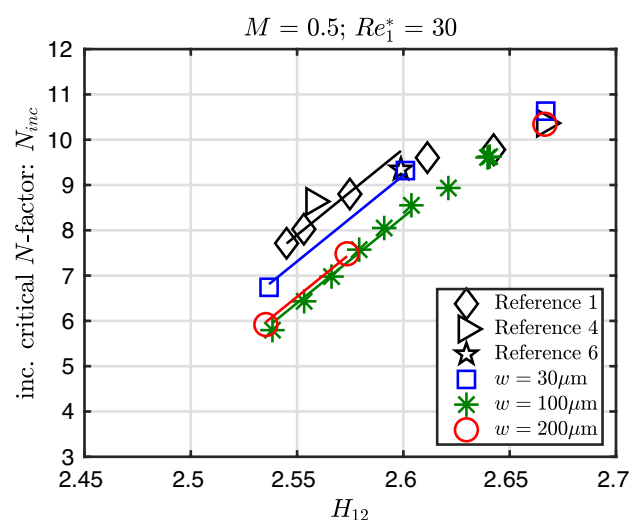


Fig. 35 Inc. critical N -factors as a function of H_{12} for different reference configurations and gap widths with $M = 0.50$, $Re_1^* = 30$

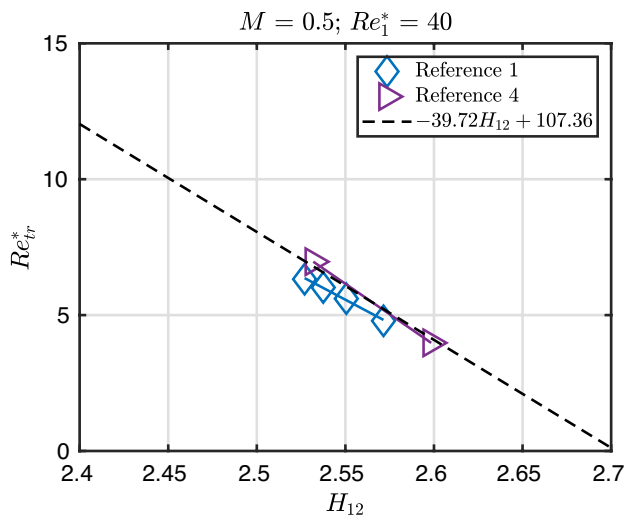


Fig. 36 Re_{tr}^* as a function of H_{12} for the reference configuration

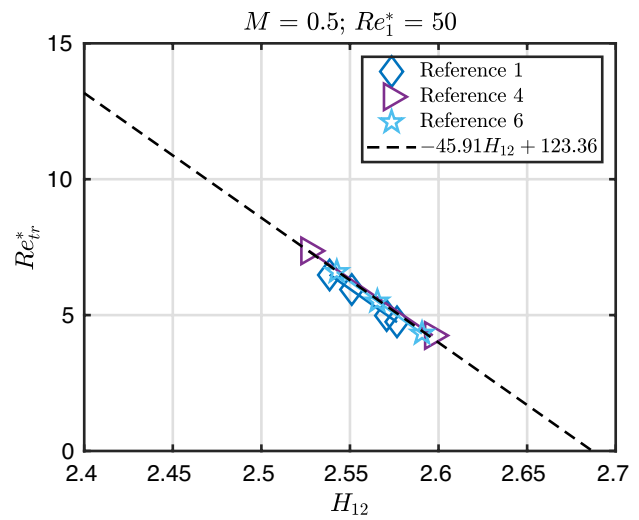


Fig. 39 Re_{tr}^* as a function of H_{12} for the reference configuration

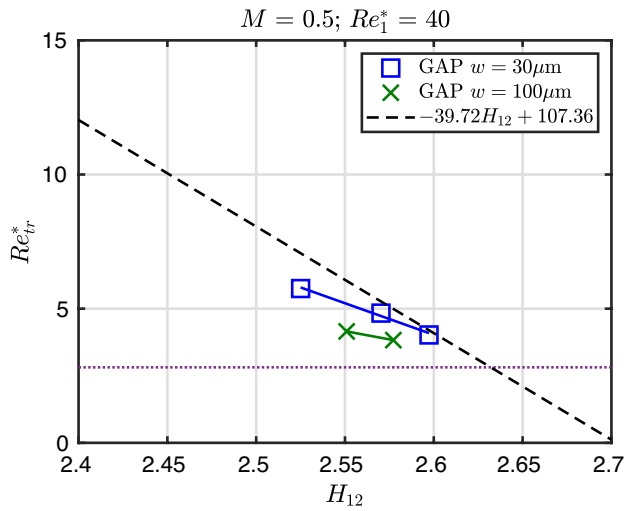


Fig. 37 Re_{tr}^* as a function of H_{12} the configurations with gaps

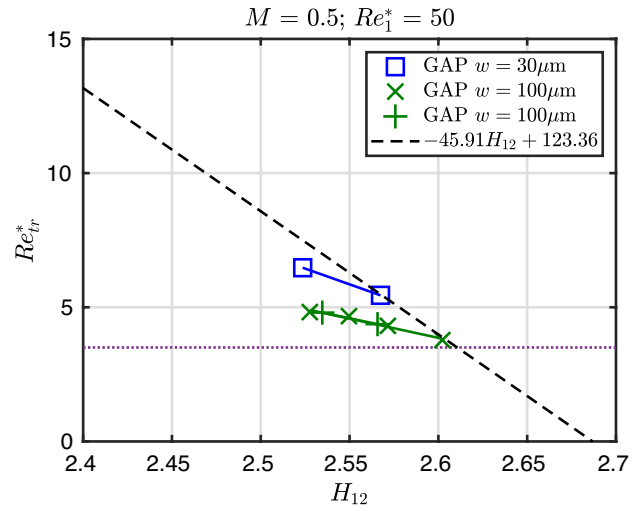


Fig. 40 Re_{tr}^* as a function of H_{12} the configurations with gaps

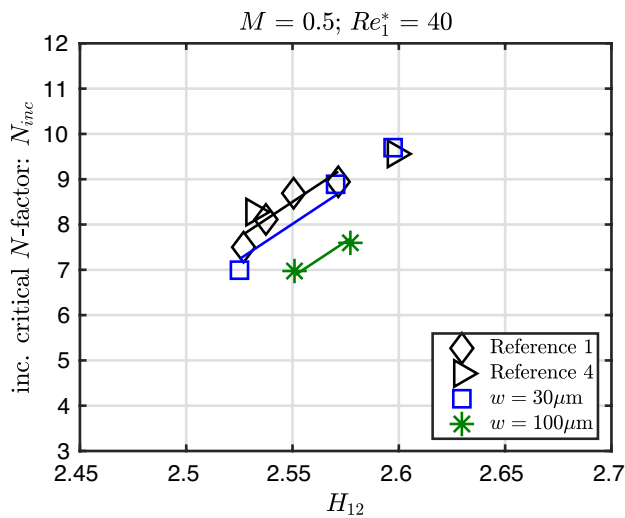


Fig. 38 Inc. critical N -factors as a function of H_{12} for different reference configurations and gap widths with $M = 0.50$, $Re_1^* = 40$

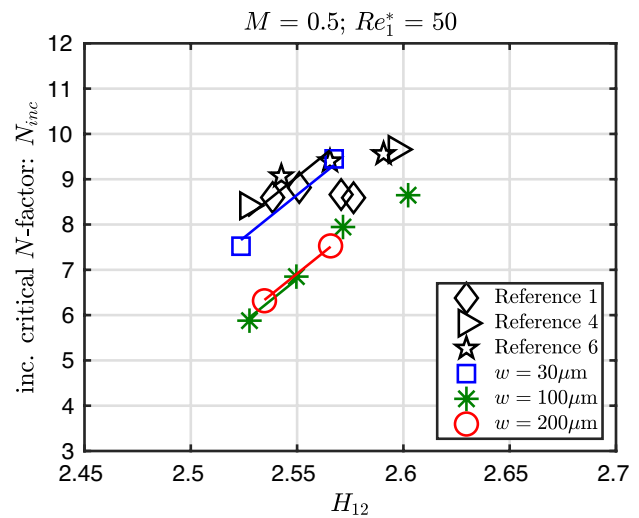


Fig. 41 Inc. critical N -factors as a function of H_{12} for different reference configurations and gap widths with $M = 0.50$, $Re_1^* = 50$

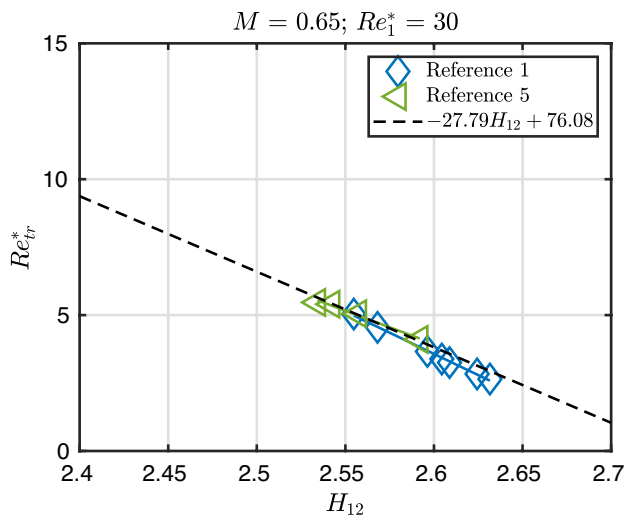


Fig. 42 Re_{tr}^* as a function of H_{12} for the reference configuration

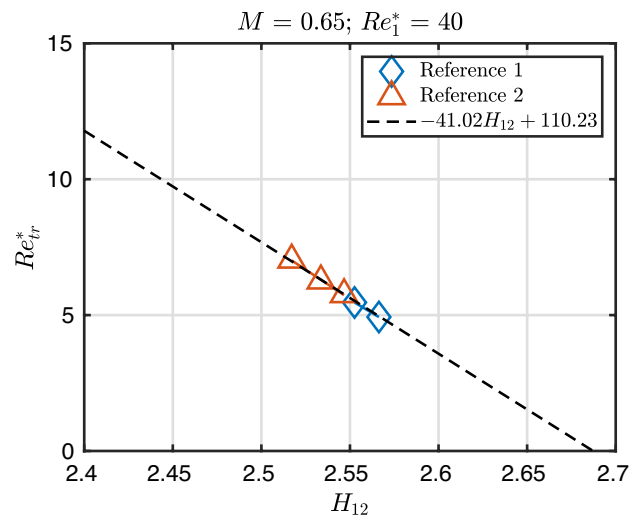


Fig. 45 Re_{tr}^* as a function of H_{12} for the reference configuration

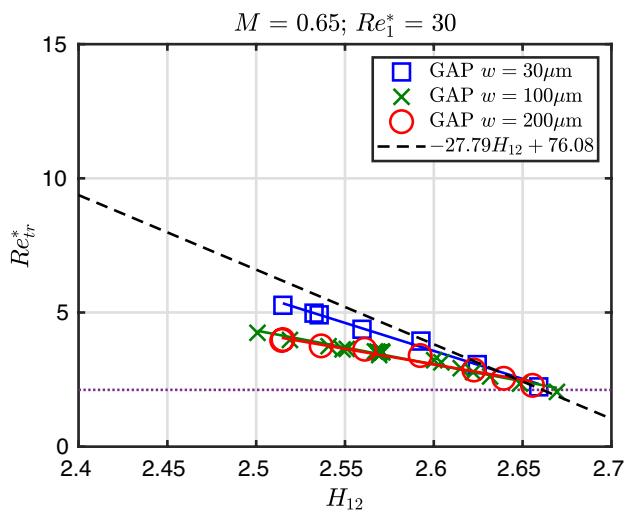


Fig. 43 Re_{tr}^* as a function of H_{12} the configurations with gaps

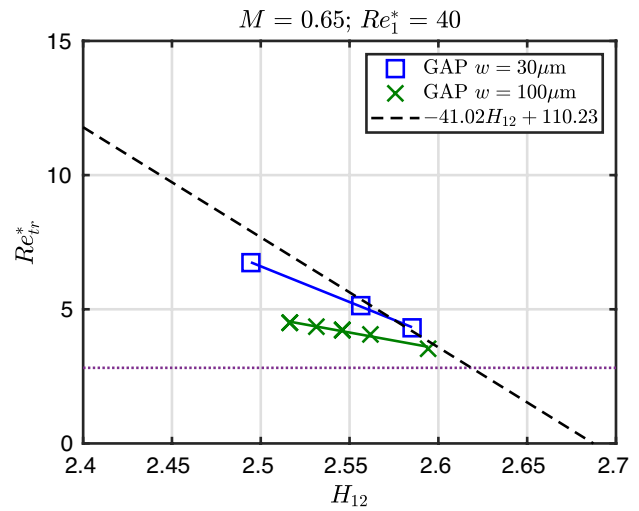


Fig. 46 Re_{tr}^* as a function of H_{12} the configurations with gaps

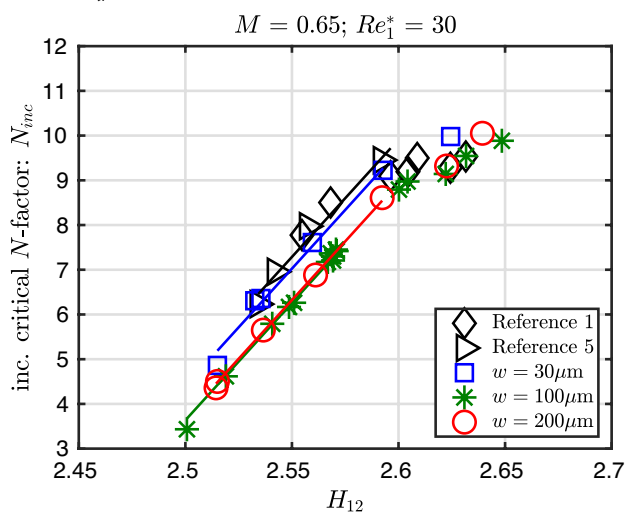


Fig. 44 Inc. critical N -factors as a function of H_{12} for different reference configurations and gap widths with $M = 0.65$, $Re_1^* = 30$

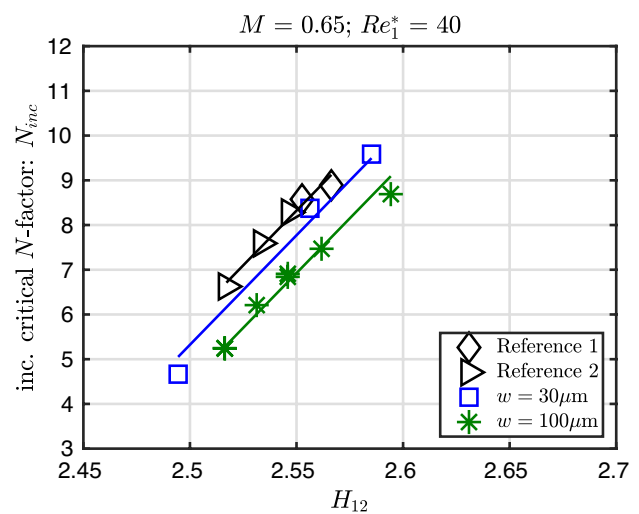


Fig. 47 Inc. critical N -factors as a function of H_{12} for different reference configurations and gap widths with $M = 0.65$, $Re_1^* = 40$

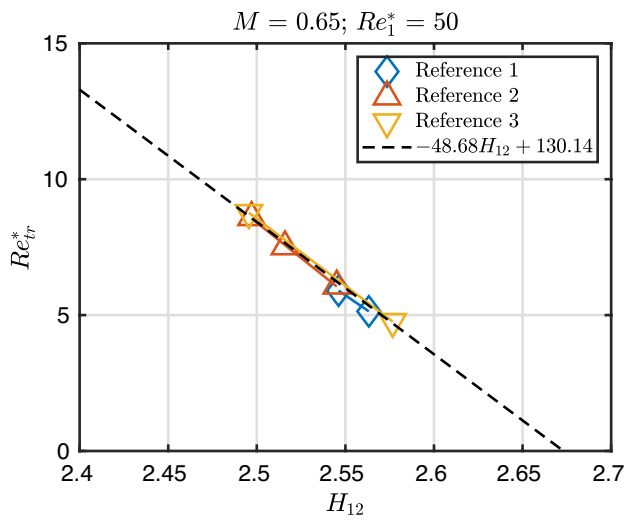


Fig. 48 Re_{tr}^* as a function of H_{12} for the reference configuration

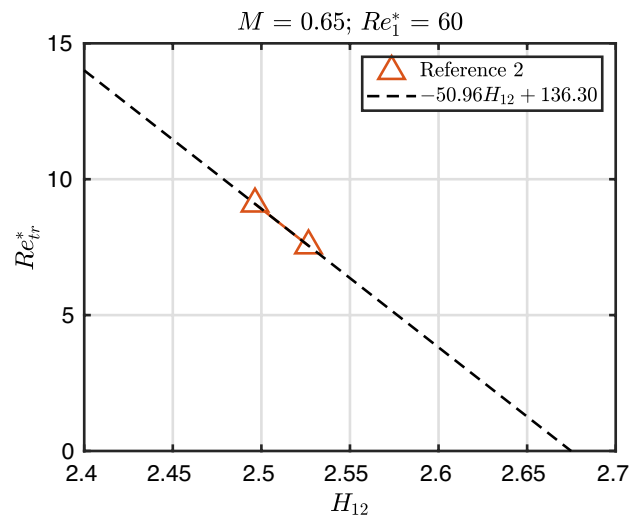


Fig. 51 Re_{tr}^* as a function of H_{12} for the reference configuration

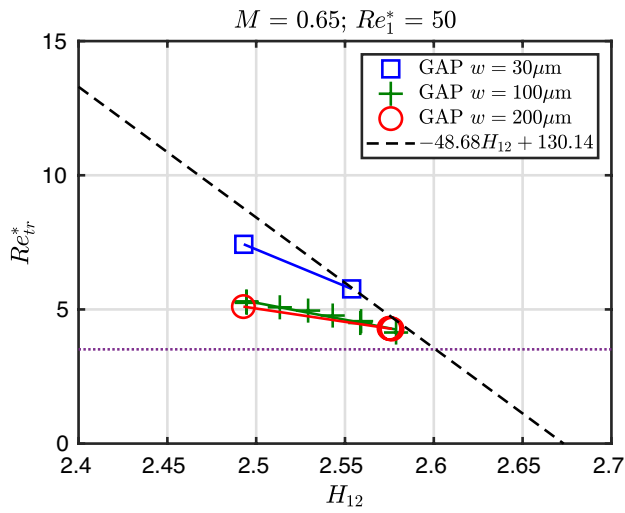


Fig. 49 Re_{tr}^* as a function of H_{12} the configurations with gaps

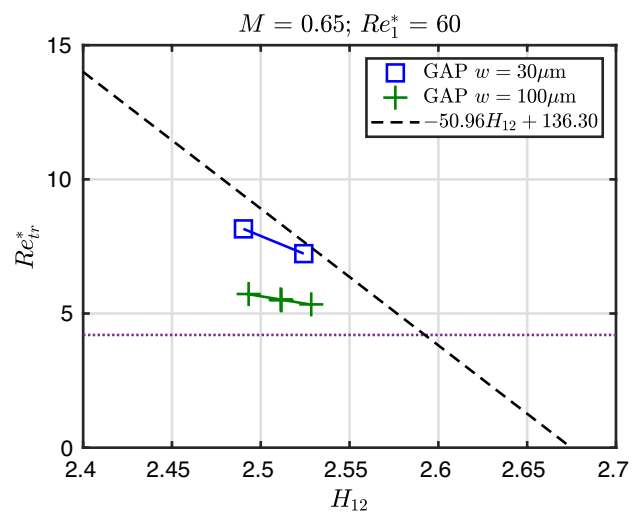


Fig. 52 Re_{tr}^* as a function of H_{12} the configurations with gaps

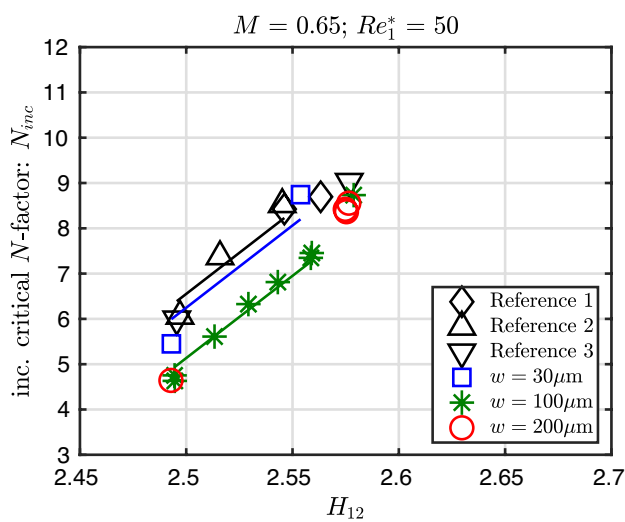


Fig. 50 Inc. critical N -factors as a function of H_{12} for different reference configurations and gap widths with $M = 0.65$, $Re_1^* = 50$

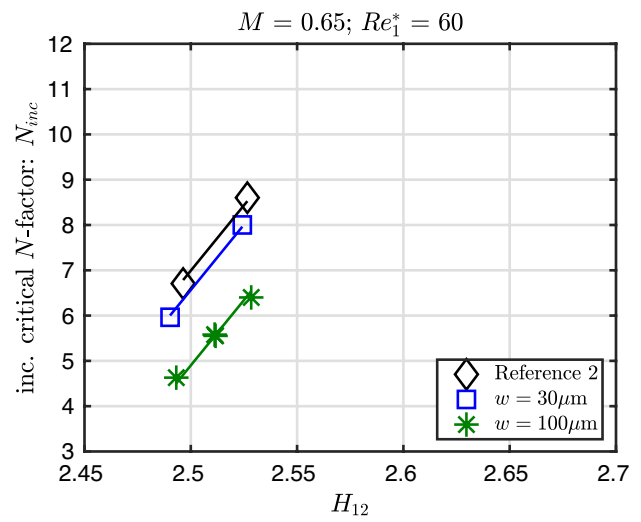


Fig. 53 Inc. critical N -factors as a function of H_{12} for different reference configurations and gap widths with $M = 0.65$, $Re_1^* = 60$

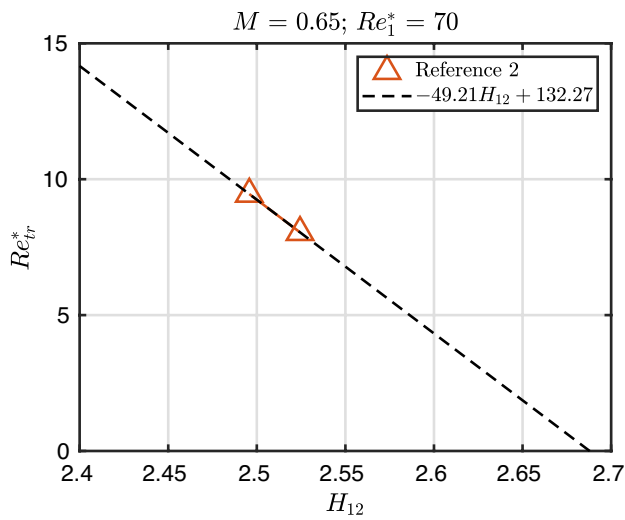


Fig. 54 Re_{tr}^* as a function of H_{12} for the reference configuration

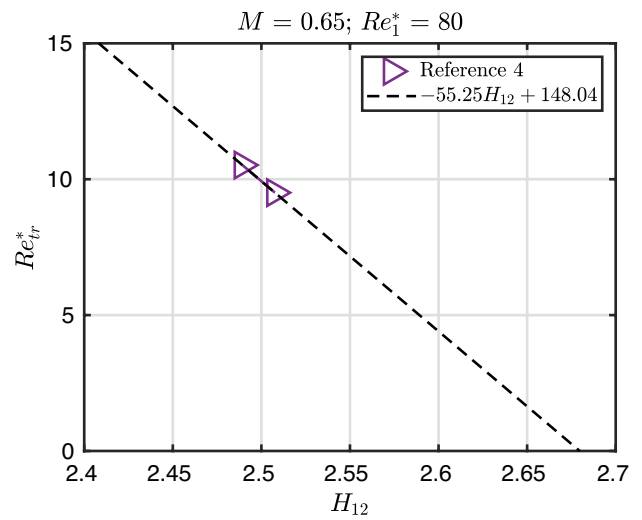


Fig. 57 Re_{tr}^* as a function of H_{12} for the reference configuration

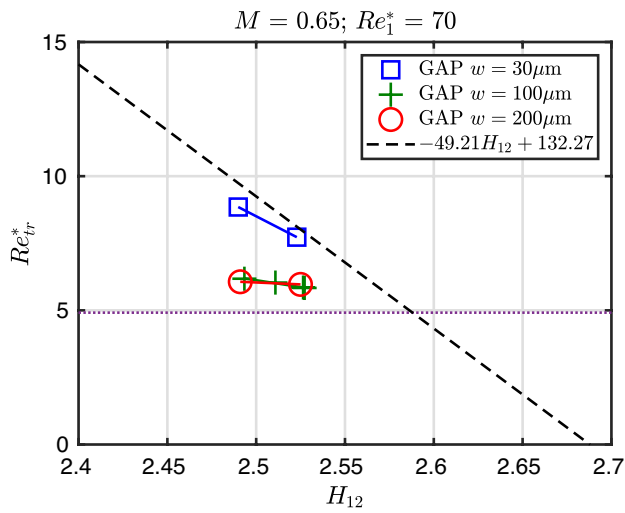


Fig. 55 Re_{tr}^* as a function of H_{12} the configurations with gaps

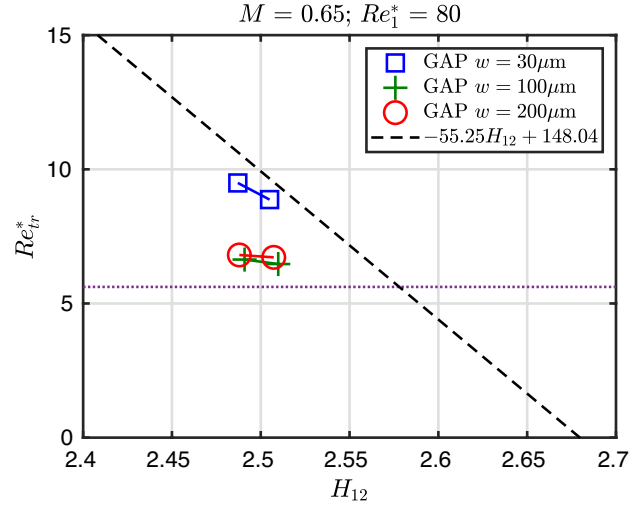


Fig. 58 Re_{tr}^* as a function of H_{12} the configurations with gaps

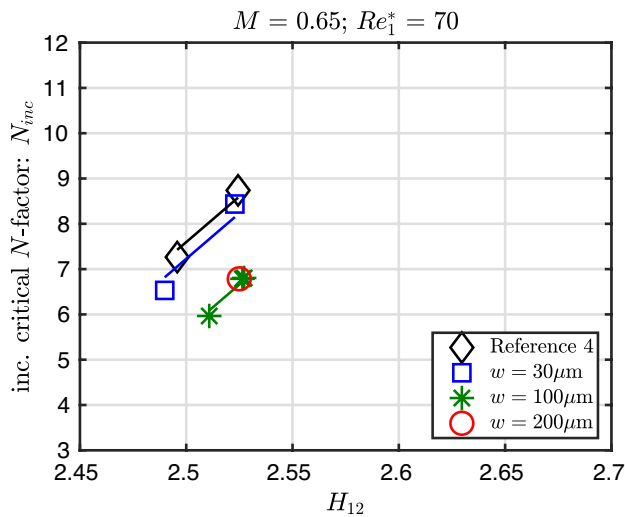


Fig. 56 Inc. critical N -factors as a function of H_{12} for different reference configurations and gap widths with $M = 0.65, Re_1^* = 70$

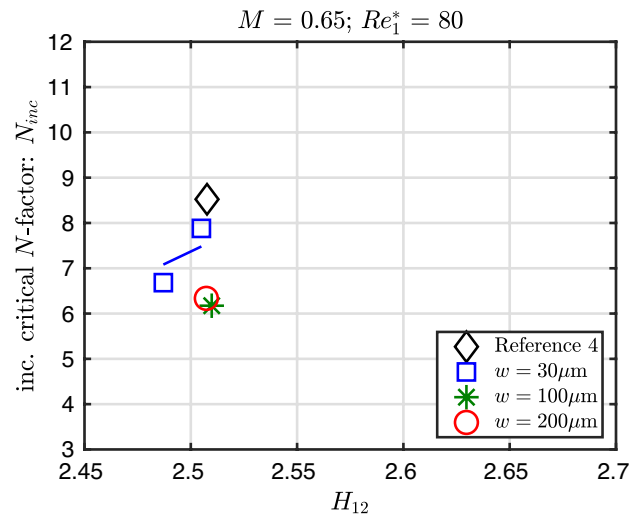


Fig. 59 Inc. critical N -factors as a function of H_{12} for different reference configurations and gap widths with $M = 0.65, Re_1^* = 80$

Table 4 Intercepts, $h_{II,0}$, of configuration with $w = 30 \mu\text{m}$ as a function of unit Reynolds number and Mach number (see Eq. II)

| Re_1^* | $M = 0.35$ | $M = 0.50$ | $M = 0.65$ |
|----------|------------|------------|------------|
| 17.5 | 22.68 | | |
| 22.5 | | 41.55 | |
| 30.0 | 51.14 | 58.71 | 57.85 |
| 40.0 | 58.24 | 65.24 | 73.18 |
| 50.0 | 64.66 | 65.68 | 75.61 |
| 60.0 | | | 75.77 |
| 70.0 | | | 93.69 |
| 80.0 | | | 95.68 |

Table 5 Intercepts, $h_{II,0}$, of configuration with $w = 100 \mu\text{m}$ as a function of unit Reynolds number and Mach number (see Eq. II)

| Re_1^* | $M = 0.35$ | $M = 0.50$ | $M = 0.65$ |
|----------|------------|------------|------------|
| 17.5 | 27.40 | | |
| 22.5 | | 30.09 | |
| 30.0 | 29.93 | 36.43 | 35.85 |
| 40.0 | 34.09 | 35.61 | 34.78 |
| 50.0 | 35.75 | 41.15 | 36.90 |
| 60.0 | | | 33.09 |
| 70.0 | | | 31.63 |
| 80.0 | | | 28.56 |

Table 6 Intercepts, $h_{II,0}$, of configuration with $w = 200 \mu\text{m}$ as a function of unit Reynolds number and Mach number (see Eq. II)

| Re_1^* | $M = 0.35$ | $M = 0.50$ | $M = 0.65$ |
|----------|------------|------------|------------|
| 17.5 | 25.55 | | |
| 22.5 | | 30.19 | |
| 30.0 | 31.63 | 38.24 | 33.03 |
| 40.0 | | | |
| 50.0 | 35.35 | | 29.86 |
| 60.0 | | | 33.09 |
| 70.0 | | | 13.25 |
| 80.0 | | | 18.21 |

Table 7 Slopes, $h_{II,1}$, of configuration with $w = 30 \mu\text{m}$ as a function of unit Reynolds number and Mach number (see Eq. II)

| Re_1^* | $M = 0.35$ | $M = 0.50$ | $M = 0.65$ |
|----------|------------|------------|------------|
| 17.5 | -7.58 (3) | | |
| 22.5 | | -14.72 (4) | |
| 30.0 | -18.20 (3) | -21.20 (3) | -20.88 (7) |
| 40.0 | -20.71 (2) | -23.55 (3) | -26.62 (3) |
| 50.0 | -23.07 (4) | -23.46 (2) | -27.35 (2) |
| 60.0 | | | -27.15 (2) |
| 70.0 | | | -34.07 (2) |
| 80.0 | | | -34.65 (2) |

For each slope the number of evaluated data points is given in brackets

Table 8 Slopes, $h_{II,1}$, of configuration with $w = 100 \mu\text{m}$ as a function of unit Reynolds number and Mach number (see Eq. II)

| Re_1^* | $M = 0.35$ | $M = 0.50$ | $M = 0.65$ |
|----------|-------------|------------|-------------|
| 17.5 | -9.46 (4) | | |
| 22.5 | | -10.49 (3) | |
| 30.0 | -10.20 (10) | -12.84 (9) | -12.61 (18) |
| 40.0 | -11.67 (7) | -12.33 (2) | -12.02 (7) |
| 50.0 | -12.17 (6) | -14.34 (4) | -12.66 (8) |
| 60.0 | | | -10.98 (4) |
| 70.0 | | | -10.20 (4) |
| 80.0 | | | -8.80 (2) |

For each slope the number of evaluated data points is given in brackets

Table 9 Slopes, $h_{II,1}$, of configuration with $w = 200 \mu\text{m}$ as a function of unit Reynolds number and Mach number (see Eq. II)

| Re_1^* | $M = 0.35$ | $M = 0.50$ | $M = 0.65$ |
|----------|------------|------------|------------|
| 17.5 | -8.80 (3) | | |
| 22.5 | | -10.49 (4) | |
| 30.0 | -10.80 (3) | -13.53 (3) | -11.53 (8) |
| 40.0 | | | |
| 50.0 | -12.04 (3) | | -9.93 (4) |
| 60.0 | | | -10.98 (4) |
| 70.0 | | | -2.88 (2) |
| 80.0 | | | -4.58 (2) |

For each slope the number of evaluated data points is given in brackets

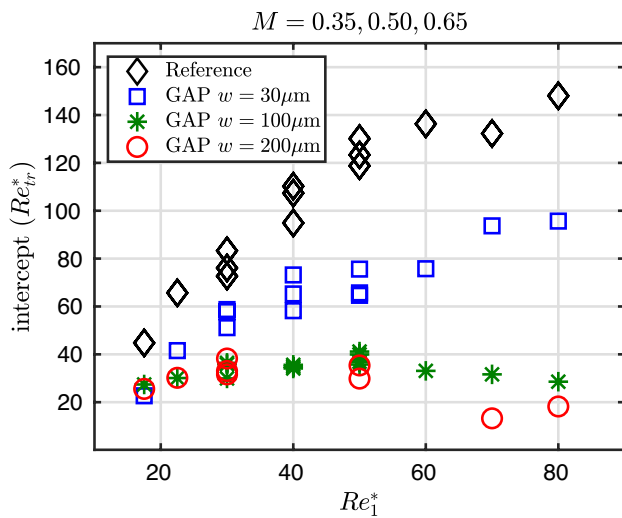


Fig. 60 Intercepts, $h_{II,0}$, of the linear approximation for all data points

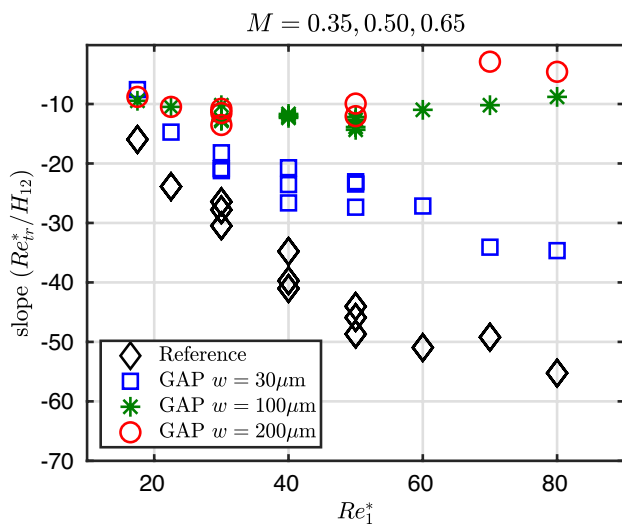


Fig. 61 Slopes, $h_{II,1}$, of the linear approximation for all data points

Acknowledgements We would like to thank A. Dillmann, L. Koop, M. Rein, H. Rosemann (all DLR) for their support and advise; U. G. Becker (DLR), C. Fuchs (DLR), T. Kleindienst (DLR), V. Ondrus (FH Münster) and L. Schojda (previously DLR) for model and test preparation; W. H. Beck, B. D. Dimond, S. Hein, U. Henne, M. Hilfer, S. Koch, J. Lemarechal, A. Weiss (all DLR) and W. E. Sachs (previously DLR) for their help during the measurement campaign, data evaluation and interpretation. Furthermore, we would like to thank M. Aschoff (DLR), S. Hücke and R. Kahle (previously DLR) for the support during the wind-tunnel test campaigns.

Author Contributions All authors contributed to the study conception and design. Material preparation, data collection and analysis were performed by Steffen Risius. The first draft of the manuscript was written by Steffen Risius, and all authors commented on previous versions of the manuscript. All authors read and approved the final manuscript.

Funding Open Access funding enabled and organized by Projekt DEAL. No funding was received to assist with the preparation of this manuscript.

Availability of data and materials The datasets generated and analysed during the current study are available from the corresponding author upon reasonable request and with permission of the German Aerospace Center (DLR).

Declarations

Ethical approval Not applicable.

Conflict of interest The authors have no competing interests to declare that are relevant to the content of this article.

Open Access This article is licensed under a Creative Commons Attribution 4.0 International License, which permits use, sharing, adaptation, distribution and reproduction in any medium or format, as long as you give appropriate credit to the original author(s) and the source, provide a link to the Creative Commons licence, and indicate if changes were made. The images or other third party material in this article are included in the article’s Creative Commons licence, unless indicated otherwise in a credit line to the material. If material is not included in the article’s Creative Commons licence and your intended use is not permitted by statutory regulation or exceeds the permitted use, you will need to obtain permission directly from the copyright holder. To view a copy of this licence, visit <http://creativecommons.org/licenses/by/4.0/>.

References

Arnal D (1989) Laminar-turbulent transition problems in supersonic and hypersonic flows. In: AGARD Special Course on Aerothermodynamics of Hypersonic Vehicles, AGARD-R-761, AGARD, Advisory Group for Aerospace Research & Development, Rhode-Saint-Genèse, Belgium, pp 8–18–45

Arnal D (1992) Boundary layer transition: prediction, application to drag reduction. Tech. Rep. AGARD Rept. 786, Advisory Group for Aerospace Research and Development

Arnal D, Casalis G, Cousteix J, Reneaux J (1997) Laminar-turbulent transition in subsonic boundary layers: research and applications in France. In: 28th fluid dynamics conference, american institute of aeronautics and astronautics. <https://doi.org/10.2514/6.1997-1905>

Beguet S, Perraud J, Forte M, Brazier JP (2017) Modeling of transverse gaps effects on boundary-layer transition. J Aircr 54(2):794–801. <https://doi.org/10.2514/1.C033647>

Costantini M (2016) Experimental analysis of geometric, pressure gradient and surface temperature effects on boundary-layer transition in compressible high Reynolds number flow. PhD thesis, RWTH Aachen University, Aachen

Costantini M, Fey U, Henne U, Klein C (2015) Nonadiabatic surface effects on transition measurements using temperature-sensitive paints. AIAA J 53(5):1172–1187. <https://doi.org/10.2514/1.J053155>

Costantini M, Risius S, Klein C (2015) Experimental investigation of the effect of forward-facing steps on boundary layer transition. Proc IUTAM 14:152–162. <https://doi.org/10.1016/j.piutam.2015.03.036>

Costantini M, Risius S, Klein C, Kühn W (2016) Effect of forward-facing steps on boundary layer transition at a subsonic Mach number. In: New results in numerical and experimental fluid mechanics x, notes on numerical fluid mechanics and

- multidisciplinary design. Springer, Cham, pp 203–213, https://doi.org/10.1007/978-3-319-27279-5_18
- Costantini M, Risius S, Klein C (2018) Non-adiabatic surface effects on step-induced boundary-layer transition. *Flow Turbul Combust* 100(4):1145–1177. <https://doi.org/10.1007/s10494-018-9913-7>
- Costantini M, Henne U, Risius S, Klein C (2021) A robust method for reliable transition detection in temperature-sensitive paint data. *Aerosp Sci Technol* 113(106):702. <https://doi.org/10.1016/j.ast.2021.106702>
- Crouch J, Kosorygin V, Ng L (2006) Modeling the effects of steps on boundary-layer transition. In: Govindarajan R (ed) IUTAM symposium on laminar-turbulent transition, fluid mechanics and its applications. Springer Netherlands, Dordrecht, pp 37–44. https://doi.org/10.1007/1-4020-4159-4_4
- Crouch JD (2022) Predicting laminar-turbulent transition influenced by surface-induced flow distortions. In: Sherwin S, Schmid P, Wu X (eds) IUTAM laminar-turbulent transition, Springer International Publishing, Cham, IUTAM Bookseries, pp 19–32. https://doi.org/10.1007/978-3-030-67902-6_2
- Crouch JD, Kosorygin VS (2020) Surface step effects on Boundary-Layer transition dominated by Tollmien-Schlichting instability. *AIAA J* 58(7):2943–2950. <https://doi.org/10.2514/1.J058518>
- Crouch JD, Kosorygin VS, Sutanto MI, Miller GD (2022) Characterizing surface-gap effects on boundary-layer transition dominated by Tollmien-Schlichting instability. *Flow 2*:E8. <https://doi.org/10.1017/flo.2022.1>
- Dimond B, Costantini M, Risius S, Fuchs C, Klein C (2019) Experimental analysis of suction on step-induced boundary-layer transition. *Exp Thermal Fluid Sci* 109(109):842. <https://doi.org/10.1016/j.expthermflusci.2019.109842>
- Dimond B, Costantini M, Risius S, Klein C, Rein M (2020) Experimental investigation of the delay of gap- and step-induced transition by means of suction. In: Dillmann A, Heller G, Krämer E, Wagner C, Tropea C, Jakirlić S (eds) New results in numerical and experimental fluid mechanics XII, Springer International Publishing, Cham, Notes on numerical fluid mechanics and multidisciplinary design, pp 165–174. https://doi.org/10.1007/978-3-030-25253-3_16
- Dimond B, Costantini M, Klein C (2021) Experimental Analysis of the Effect of Suction and Step Height on Boundary-Layer Transition. In: Sherwin S, Schmid P, Wu X (eds) IUTAM laminar-turbulent transition, Springer International Publishing, Cham, IUTAM Bookseries, pp 171–180. https://doi.org/10.1007/978-3-030-67902-6_14
- EASA (2017) Type-Certificate Data Sheet No. EASA.A.064 - Airbus A318, A319, A320, A321
- EASA (2023) Type-Certificate Data Sheet No. EASA.IM.A.120 - Boeing 737
- Edelmann CA, Rist U (2015) Impact of forward-facing steps on laminar-turbulent transition in transonic flows. *AIAA J* 53(9):2504–2511. <https://doi.org/10.2514/1.J053529>
- Egami Y, Fey U, Klein C, Quest J, Ondrus V, Beifuss U (2012) Development of new two-component temperature-sensitive paint (TSP) for cryogenic testing. *Meas Sci Technol* 23(11):115,301. <https://doi.org/10.1088/0957-0233/23/11/115301>
- Forte M, Perraud J, Seraudie A, Beguet S, Casalis L, Gentili G (2015) experimental and numerical study of the effect of gaps on laminar turbulent transition of incompressible boundary layers. *Procedia IUTAM* 14:448–458. <https://doi.org/10.1016/j.piutam.2015.03.073>
- Franco JA, Hein S, Valero E (2018) Effect of humps and indentations on boundary-layer transition of compressible flows using the AHLNS methodology. In: 7th European conference on computational fluid dynamics (ECFD 7)
- Franco JA, Theiss A, Hein S (2021) Influence of surface irregularities on the expected Boundary-Layer transition location on hybrid laminar flow control wings. In: Dillmann A, Heller G, Krämer E, Wagner C (eds) New results in numerical and experimental fluid mechanics XIII, vol 151, Springer International Publishing, Cham, pp 174–184. https://doi.org/10.1007/978-3-030-79561-0_17
- Hensch AK, Guntermann P, Longo R, Klein C, Risius S, Schaber S, Quest J, Okfen P (2019) Investigation of Hybrid Laminar Flow Control (HLFC) on a 2D-model in the cryogenic pilot European Transonic Windtunnel (PETW). In: AIAA Scitech 2019 Forum, AIAA SciTech Forum, American Institute of Aeronautics and Astronautics, <https://doi.org/10.2514/6.2019-1181>
- Holmes B, Croom C, Gail P, Manuel G, Carraway D (1986) Advanced boundary layer transition measurement methods for flight applications. In: AIAA, American institute of aeronautics and astronautics, <https://doi.org/10.2514/6.1986-9786>
- Koch S (2004) Zeitliche und räumliche Turbulenzentwicklung in einem Rohrwindkanal und deren Einfluss auf die Transition an Profilmödeln. PhD thesis, Georg-August-University, Göttingen
- Liu T, Sullivan JP, Asai K, Klein C, Egami Y (2021) Pressure and temperature sensitive paints, 2nd edn. Springer, New York
- Masad JA, Nayfeh AH (1992) Effect of a bulge on the subharmonic instability of subsonic boundary layers. *AIAA J* 30(7):1731–1737. <https://doi.org/10.2514/3.11130>
- Methel J, Forte M, Vermeersch O, Casalis G (2022) Experimental investigation on the effect of forward-facing steps and gaps combined with wall suction on boundary layer transition. *Exp Fluids* 63(1):21. <https://doi.org/10.1007/s00348-021-03361-x>
- Nenni JP, Gluyas GL (1966) Aerodynamic design and analysis of an LFC surface. *Astronaut Aeronaut* 4(7):52–57
- Ondrus V, Meier RJ, Klein C, Henne U, Schäferling M, Beifuss U (2015) Europium 1,3-di(thienyl)propane-1,3-diones with outstanding properties for temperature sensing. *Sens Actuators A* 233:434–441. <https://doi.org/10.1016/j.sna.2015.07.023>
- Perraud J, Séraudie A (2000) Effects of Steps and Gaps on 2D and 3D Transition. In: European congress on computational methods in applied sciences and engineering, p 18
- Reichstein T, Schaffarczyk AP, Dollinger C, Balaresque N, Schülein E, Jauch C, Fischer A (2019) Investigation of laminar-turbulent transition on a rotating Wind-Turbine blade of multimegawatt class with thermography and microphone array. *Energies* 12(11):2102. <https://doi.org/10.3390/en12112102>
- Risius S (2014) Entwurf eines Messsystems zur instationären quantitativen TSP Messung am kryogenen Rohrwindkanal Göttingen (KRG). *Berichtsreihe DLR-IB 224-2014 A 103*, German Aerospace Center, DLR
- Risius S (2018) Development of a time-resolved quantitative surface-temperature measurement technique and its application in short-duration wind tunnel testing. PhD thesis, Georg-August-University Göttingen
- Risius S, Costantini M, Kleindienst T (2015) Untersuchung optischer Komponenten (LEDs und Filter) für den Einsatz bei kryoTSP und warmTSP. *Berichtsreihe 224-2015 A 113*, German Aerospace Center, DLR
- Risius S, Costantini M, Hein S, Koch S, Klein C (2018a) Experimental investigation of Mach number and pressure gradient effects on boundary layer transition in two-dimensional flow. In: New results in numerical and experimental fluid mechanics XI, Notes on Numerical Fluid Mechanics and Multidisciplinary Design, Springer, Cham, pp 305–314. https://doi.org/10.1007/978-3-319-64519-3_28
- Risius S, Costantini M, Koch S, Hein S, Klein C (2018) Unit Reynolds number, Mach number and pressure gradient effects on laminar-turbulent transition in two-dimensional boundary layers. *Exp Fluids*. <https://doi.org/10.1007/s00348-018-2538-8>

- Rius-Vidales AF, Kotsonis M (2021) Impact of a forward-facing step on the development of crossflow instability. *J Fluid Mech.* <https://doi.org/10.1017/jfm.2021.497>
- Rosemann H (1997) The cryogenic Ludwig-tube tunnel at Göttingen. In: Special course on advances in cryogenic wind tunnel technology, no. R-812 in AGARD, AIAA, Neuilly-sur-Seine, pp 8–1–8–13
- Schlichting H, Gersten K, Krause E, Oertel HJ (2006) *Grenzschicht-Theorie*, 10th edn. Springer, Berlin
- Schrauf G (1998) COCO-A program to compute velocity and temperature profiles for local and nonlocal stability analysis of compressible, conical boundary layers with suction. ZARM Technik report
- Schrauf G (2005) Status and perspectives of laminar flow. *Aeronaut J* 109(1102):639–644. <https://doi.org/10.1017/S000192400000097X>
- Schrauf G (2006) LILO 2.1 User's guide and tutorial. Bremen, Germany, GSSC Technical Report 6
- Smith AMO, Gamberoni N (1956) Transition, pressure gradient, and stability theory. Tech. Rep. ES. 26388, Douglas Aircraft Co Inc, El Segundo, CA
- Tocci F, Franco JA, Hein S, Chauvat G, Hanifi A (2021a) The effect of 2-D surface irregularities on laminar-turbulent transition: a comparison of numerical methodologies. In: Dillmann A, Heller G, Krämer E, Wagner C (eds) *New results in numerical and experimental fluid mechanics XIII*, vol 151, Springer International Publishing, Cham, pp 246–256, https://doi.org/10.1007/978-3-030-79561-0_24
- Tocci F, Franco JA, Hein S, Chauvat G, Hanifi A (2021b) The effect of 2-D surface irregularities on laminar-turbulent transition: a comparison of numerical methodologies. In: Dillmann A, Heller G, Krämer E, Wagner C (eds) *New results in numerical and experimental fluid mechanics XIII*, Springer International Publishing, Cham, Notes on Numerical Fluid Mechanics and Multidisciplinary Design, pp 246–256, https://doi.org/10.1007/978-3-030-79561-0_24
- Traphan D, Meinschmidt P, Schlüter F, Lutz O, Peinke J, Gülker G (2015) High-speed measurements of different laminar-turbulent transition phenomena on rotor blades by means of infrared thermography and stereoscopic PIV. In: 10th Pacific symposium on flow visualization and image processing, p 11
- van Ingen J (1956) A suggested semi-empirical method for the calculation of the boundary layer transition region. Tech. Rep. Rapport VTH-74, Technische Hogeschool Delft, Vliegtuigbouwkunde, Delft
- Wang YX, Gaster M (2005) Effect of surface steps on boundary layer transition. *Exp Fluids* 39(4):679–686. <https://doi.org/10.1007/s00348-005-1011-7>
- Zahn J, Rist U (2015) Impact of deep gaps on laminar-turbulent transition in compressible boundary-layer flow. *AIAA J* 54(1):66–76. <https://doi.org/10.2514/1.J054112>
- Zahn J, Rist U (2017) Active and natural suction at forward-facing steps for delaying laminar-turbulent transition. *AIAA J* 55(4):1343–1354. <https://doi.org/10.2514/1.J055122>

Publisher's Note Springer Nature remains neutral with regard to jurisdictional claims in published maps and institutional affiliations.